Acta Materialia 226 (2022) 117602

Contents lists available at ScienceDirect

Acta Materialia

journal homepage: www.elsevier.com/locate/actamat

Full length article

CALPHAD-informed phase-field model for two-sublattice phases based on chemical potentials: η-phase precipitation in Al-Zn-Mg-Cu alloys

Chuanlai Liu[a,*], Alec Davis[b,c], Jonathan Fellowes[d], Philip B. Prangnell[b,c], Dierk Raabe[a], Pratheek Shanthraj[b,c,*]

[a] Max-Planck-Institut für Eisenforschung GmbH, Max-Planck-Str. 1, Düsseldorf 40237, Germany
[b] Department of Materials, The University of Manchester, Manchester M13 9PL, UK
[c] Henry Royce Institute for Advanced Materials, The University of Manchester, Manchester, M13 9PL, UK
[d] Department of Earth and Environmental Sciences, The University of Manchester, Manchester M13 9PL, UK

ARTICLE INFO

Article history:
Received 14 September 2021
Revised 28 November 2021
Accepted 28 December 2021
Available online 31 December 2021

Keywords:
Phase-field
CALPHAD
Two-sublattice phase
Multi-component diffusion
Al-Zn-Mg-Cu alloy

ABSTRACT

The electrochemical properties of high strength 7xxx aluminium alloys strongly depend on the substitutional occupancy of Zn by Cu and Al in the strengthening η-phase with the two-sublattice structure, and its microstructural and compositional prediction is the key to design of new generation corrosion resistant alloys. In this work, we have developed a chemical-potential-based phase-field model capable of describing multi-component and two-sublattice ordered phases, during commercial multi-stage artificial ageing treatments, by directly incorporating the compound energy CALPHAD formalism. The model developed has been employed to explore the complex compositional pathway for the formation of the η-phase in Al-Zn-Mg-Cu alloys during heat treatments. In particular, the influence of alloy composition, solute diffusivity, and heat treatment parameters on the microstructural and compositional evolution of η-phase precipitates, was systematically investigated from a thermodynamic and kinetic perspective and compared to electron probe microanalysis validation data. The simulated η-phase growth kinetics and the matrix residual solute evolution in the AA7050 alloy indicates that Zn depletion mainly controlled the η-phase growth process during the early stage of ageing, resulting in fast η-phase growth kinetics, enrichment of Zn in the η-phase, and an excess in residual Cu in the matrix. The gradual substitution of Zn by Cu atoms in the η-phase during the later ageing stage was in principle a kinetically controlled process, owing to the slower diffusivity of Cu relative to Zn in the matrix. It was also found that the higher nominal Zn content in alloys like the AA7085 alloy, compared to the AA7050 alloy, could significantly enhance the chemical potential of Zn, but this had a minor influence on Cu, which essentially led to the higher Zn content (and consequently lower Cu) seen in the η-phase. Finally, substantial depletion of Zn and supersaturation of Cu in the matrix of the AA7050 alloy was predicted after 24 h ageing at 120 °C, whereas the second higher-temperature ageing stage at 180 °C markedly enhanced the diffusion of Cu from the supersaturated matrix into the η-phase, while the matrix residual Zn content was only slightly affected.

1. Introduction

Ordered solid solution phases play a fundamental role in determining the mechanical, electrochemical, and environmental properties of metallic alloys, such as γ' precipitates in Ni-based superalloys [1] and η' (and η) precipitates in 7xxx aluminium (Al) alloys (Al-Zn-Mg-(Cu) system) [2–13]. These structural alloys are usually multi-component in nature containing many deliberate alloying additions and impurity elements. Furthermore, the present strengthening phases have ordered lattice structures, wherein elemental site preference arises [10]. The microstructural characteristics of these ordered phases, *e.g.* composition, size distribution, morphologies, number density, and the related remaining solute levels in the matrix are comprehensively determined by alloy composition and complex thermal process kinetic pathways [14]. Therefore, quantitative design and optimization in a given commercial alloy system, with improved properties to meet the demanding challenges in performance and sustainability, requires the ability to

* Corresponding authors.
E-mail addresses: c.liu@mpie.de (C. Liu), pratheek.shanthraj@manchester.ac.uk (P. Shanthraj).

https://doi.org/10.1016/j.actamat.2021.117602

correctly predict and control the compositional and microstructural evolution of the complex ordered phases that dominate their properties.

The superior strength of Cu containing 7xxx series Al alloys is principally ascribed to the development of a high density of nanoscale precipitates, which undergoe the sequence from Guinier-Preston (GP) Zones to metastable η', and stable η-precipitates [3–12]. In practice, these alloys are primarily used in an overaged temper state (*e.g.* T7651, T7451 tempers) to improve their stress corrosion cracking (SCC) susceptibility at the expense of a modest loss of yield strength [15], which is accompanied by Cu enrichment in the η-phase [16,17]. It has been widely reported that the substitution of Zn by Cu in the η-phase can effectively minimise the extent of anodic dissolution of the η-phase, due to a reduced electrochemical potential difference between the matrix Al-solid solution and the Cu-containing η-phase, while the breakdown potential of the η-phase in deaerated 0.5 M NaCl is relatively unaffected by Al incorporation in the η-phase [18,19]. It is known that the η-phase is based upon its Laves-C14 crystal structure $(Al,Cu,Mg,Zn)_2(Al,Cu,Mg,Zn)_1$ with two sublattices, and the Mg concentration is generally fixed at 33.3 at.%, but both Al and Cu can substitute on the Zn lattice sites and its composition evolves during ageing heat treatments, with the Cu content increasing more slowly than that of the other species due to its lower diffusivity [16,20,21]. However, the quantitative role of the heat treatment process parameters on the solute distribution between the η-phase and matrix still remains elusive. The composition of the η-phase is furthermore determined by the bulk thermodynamic properties (*e.g.* chemical driving force, elastic strain energy), thermodynamic capillarity properties (interfacial energy, *i.e.* Gibbs-Thomson effect), and the kinetics of the phase transformation process (*e.g.* diffusivity of different solute elements). As a consequence, η-phase transformation in multi-component 7xxx Al alloys can take complex kinetic pathways, that depend on the alloy chemistry and the thermal path. It is therefore important to be able to simulate and better understand the impact of alloy composition and heat treatment on the composition and morphological characteristics (size, volume fraction, precipitate size distribution) of the η-phase precipitates and ultimately how this impacts on the materials' mechanical and corrosion properties.

The compositional evolution and particle size distribution of ordered phases in multi-component alloys is generally influenced by a number of diffusion-related processes with different elemental diffusivities, such as solute transport in the matrix, which affects the growth and coarsening behaviour of particles of various sizes. A number of theoretical and numerical frameworks have be developed to model such behaviours with varying levels of physical detail and across multiple length scales: for instance, first principles-informed lattice kinetic Monte Carlo studies on solute clustering during the early-stage precipitation [3,14], sharp interface modelling of precipitate growth kinetics [22], and mean-field Ostwald ripening theories considering a statistically relevant number of precipitates [23]. Phase-field models are effective in describing the evolution of complex microstructures and solute distributions, where adjacent compositional enrichment and depletion zones interact and where elasto-plastic deformation fields arising from the phase transformation eigenstrains gain relevance [24–31]; however, a challenge of applying such methods for the prediction of the precipitation kinetics in typical engineering alloys lies in dealing with the existence of multi-component elements and the complex multi-sublattice crystal structures of ordered phases.

In multi-component alloys, an accurate description of the Gibbs free energy and solute migration energy is paramount for quantitative phase-field simulations, since they determine precipitate compositions, volume fractions, the chemical driving force of phase transformation, and solute diffusion kinetics. CALPHAD-based thermodynamic databases have been successfully developed to model these key thermodynamic parameters and are widely used for equilibrium phase diagram calculations [32], which can be extended to non-equilibrium systems via combination with diffusion simulations [33]. The incorporation of CALPHAD databases into phase-field methods can hence remarkably enhance the capability of phase-field models to quantitatively simulate the more complex microstructure evolution found in many technologically relevant alloy systems that contain ordered solid-solution phases [34,35]. However, the direct incorporation of the CALPHAD-based Gibbs free energy formalism in phase-field methods generally suffers from poor numerical convergence and performance owing to the ill-posedness of the logarithm term in the dilute limit representing the entropic contribution [36], and the complexity of the diffuse interface equilibrium condition in multi-component systems [37]. Furthermore, the Gibbs free energy of the ordered phase is usually modelled as a function of site fractions in each sublattice and, hence, additional constrained energy minimization is required to find the site fractions for a given set of mole fractions [32]. Therefore, direct adoption of multi-sublattice models for ordered phases can further compound the computational complexity of CALPHAD/phase-field coupling.

The incorporation of multi-sublattice CALPHAD models into phase-field theories has consequently been achieved through different approaches with varying degrees of fidelity. For example, direct linking of the CALPHAD databases to phase-field simulations has been frequently performed by running a commercial CALPHAD software and the phase-field calculations interactively [34,38]. Despite being accurate, this approach is computationally intensive. Alternatively, the related thermodynamic quantities and equilibrium conditions can be pre-calculated and stored in a database prior to phase-field simulation [39]. However, their extension to multi-component systems has proven to be unfeasible, as the number of storage and data retrieval operations for thermodynamic entries increase exponentially with the number of components. In addition, polynomial fitting or piecewise approximation of the Gibbs free energy have also been commonly used in binary or ternary cases [40,41]. However, only a narrow range of the thermodynamic function can be accurately fitted by a polynomial, while the actual kinetic pathways for precipitation in complex multi-component alloys can lead to much larger compositional ranges. It is thus difficult to identify beforehand the most relevant composition window to be considered in the phase-field simulation. The direct incorporation of the multi-sublattice formalism into the phase-field model has been pursued by Zhang et al. [42], where the relationship between the specific site fractions and mole fractions was established through the finite interface dissipation method [43]. Zhu et al. [35] first proposed an approach to incorporate a four-sublattice model by relating the site fractions to the order parameters in a Ni-Al binary system, which has been recently extended to the study of multi-component Ni-based superalloys [44,45] and light-weight steels [46,47]. However, with an increasing number of elements in the alloy system, the strong coupling between the site fraction and the order parameter can escalate the mathematical complexity and hence result in intensive numerical computation. Furthermore, this method has been limited to specific applications where a single function formalism of the Gibbs energies can be adopted for both the ordered and disordered phases [44].

In order to simplify the implementation of the interface equilibrium condition, Plapp [48] has recently formulated a phase-field model based on a grand potential functional. However, to date the application of such an approach has been limited to simple binary or ternary substitutional phases [49,50], since the grand potential of the bulk phases was calculated by a Legendre transformation of the Gibbs free energy, which is mathematically unfeasible for ordered phases described by a multi-sublattice for-

malism. Furthermore, the Legendre transformation does not even exist for non-convex Gibbs free energy forms. More recently, a chemical-potential-based phase-field model has been constructed using a time-discrete semi-analytical inversion of the thermodynamic relations by the current authors [13,31]. Such an approach has the advantage that it is applicable to general CALPHAD Gibbs free energy forms of multi-component substitutional systems. This model has been used to successfully study the grain boundary η-phase transformation and microchemistry evolution in Al-Zn-Mg-Cu alloys. However, the η-phase was simplified as a stoichiometric phase and had a fixed composition throughout the heat treatment simulations [13]. The influence of alloy composition, solute diffusivity, and heat treatment parameters on the microstructural and compositional evolution of the η-phase could thus not be comprehensively investigated.

This work therefore aims to develop a chemical-potential-based phase-field model capable of describing multi-component ordered phases by directly integrating the two-sublattice CALPHAD formalism. This has been achieved by semi-analytically inverting the Gibbs free energy formulation of the ordered phase, which results in solute transport equations as a function of the chemical potentials instead of compositions. The site fraction occupied by an element in each sublattice can then be directly obtained from the dynamic variable (*i.e.* the chemical potentials). Additional computation-intensive energy minimization can thus be avoided. We begin by first describing the thermodynamics and multi-phase-field model adopted for the multi-component and two-sublattice phase, and then present an efficient numerical algorithm to solve the resulting formulation as a function of phase-field order parameters and chemical potentials. After developing the framework, we then explore the complex compositional pathway for the formation of the η-phase in Al-Zn-Mg-Cu alloys, focusing on the influence of alloy composition, solute diffusivity, and heat treatment parameters on the evolution of the η-phase composition during η-phase growth and Ostwald coarsening. Although this work has focused on the Al-Zn-Mg-Cu system, our model is built on the CALPHAD thermodynamic formulation that should facilitate generalization to many other multi-component alloy systems with multi-sublattice ordered phases.

2. Model formulation

In this section, we begin by first briefly reviewing the multi-phase-field model [25,38,51–53], and then describe the approach used to directly incorporate the CALPHAD-based multi-component and two-sublattice free energies into the formulation.

2.1. Multi-phase-field model

Assuming a multi-phase, multi-component system with $\alpha = 1 \dots N$ phases and $i = 1 \dots K$ components, the local volume fraction and solute composition for each phase are represented by the vector-valued phase fields $\boldsymbol{\varphi}$ and phase compositions $\mathbf{c}^{\alpha}$, respectively. The order parameters and phase composition meet the following constraints,

$$\sum_{\alpha}^{N} \varphi^{\alpha} = 1, \quad \text{and} \quad \sum_{\alpha}^{N} \varphi^{\alpha} c_i^{\alpha} = c_i. \tag{1}$$

The Gibbs free energy functional of this system is expressed as a function of phase fields $\boldsymbol{\varphi}$, phase compositions $\mathbf{c}^{\alpha}$, and temperature T:

$$\mathcal{F}(\boldsymbol{\varphi}, \nabla\boldsymbol{\varphi}, \mathbf{c}^{\alpha}, \mathrm{T}) = \int_V \Big(f_{\mathrm{intf}}(\boldsymbol{\varphi}, \nabla\boldsymbol{\varphi}) + f_{\mathrm{bulk}}(\boldsymbol{\varphi}, \mathbf{c}^{\alpha}, \mathrm{T}) \Big) \mathrm{d}V, \tag{2}$$

where V is the domain of consideration, f_{intf} and f_{bulk} describes the interfacial and bulk free energy density, respectively.

The interface energy density is defined by:

$$f_{\mathrm{intf}}(\boldsymbol{\varphi}, \nabla\boldsymbol{\varphi}) = \sum_{\alpha\neq\beta}^{N} \frac{4\sigma^{\alpha\beta}}{\eta^{\alpha\beta}} \left[-\frac{\eta^{\alpha\beta 2}}{\pi^2} \nabla\varphi^{\alpha} \cdot \nabla\varphi^{\beta} + \varphi^{\alpha}\varphi^{\beta} \right], \tag{3}$$

where, $\sigma^{\alpha\beta}$ and $\eta^{\alpha\beta}$ is the interface energy and width between phases α and β, respectively.

The bulk free energy includes both the elastic strain energy (f_{elas}) and chemical free energy (f_{chem}) contributions. Since η-precipitates generally have semi-coherent or incoherent precipitate-matrix interfaces [11,12], the elastic strain energy is only expected to play a minor role in the η-phase formation (see details in Section S.1 in the supplementary material). Therefore, it is physically reasonable to neglect the mechanical driving force for the present application to the simulation of η-phase growth in Al-Zn-Mg-Cu alloys. The diffuse interface is approximated as a mixture of multiple phases that each retain their macroscopic properties with the same diffusion potential. The chemical free energy density, $f_{\mathrm{chem}}(\boldsymbol{\varphi}, \mathbf{c}^{\alpha}, \mathrm{T})$, is calculated as the volume average of each phase, $f_{\mathrm{chem}}^{\alpha}(\mathbf{c}^{\alpha}, \mathrm{T})$.

The temporal and spatial evolution of the phase fields is obtained by the minimization of the total Gibbs free energy, $\mathcal{F}$, through over-damped relaxation:

$$\dot{\varphi^{\alpha}} = -\sum_{\beta=1}^{\tilde{N}} \frac{M^{\alpha\beta}}{\tilde{N}} \left[\frac{\delta\mathcal{F}}{\delta\varphi^{\alpha}} - \frac{\delta\mathcal{F}}{\delta\varphi^{\beta}} \right], \tag{4}$$

where $\tilde{N}$ is the number of active phases, $M^{\alpha\beta}$ is the interface mobility between phase α and β.

2.2. Multi-component diffusion

In the mass conservation law, a linear flux formalism is assumed for the component diffusion,

$$\dot{c}_i(\tilde{\boldsymbol{\mu}}) = \nabla \cdot \sum_{j=1}^{K-1} L_{ij}^{K} \nabla\tilde{\mu}_j, \tag{5}$$

where the vector-valued quantity, $\tilde{\boldsymbol{\mu}}$, denotes the diffusion potential of solutes. The diffusion potential of solute i, $\tilde{\mu}_i = \tilde{\mu}_i^{\alpha} = \tilde{\mu}_i^{\beta}$, is calculated as the difference of the chemical potential relative to the solvent component K:

$$\tilde{\mu}_i^{\alpha} = \left(\frac{\partial f_{\mathrm{chem}}^{\alpha}}{\partial c_i^{\alpha}} \right)_{\mathrm{T,P},c_j\neq c_i} - \left(\frac{\partial f_{\mathrm{chem}}^{\alpha}}{\partial c_K^{\alpha}} \right)_{\mathrm{T,P},c_j\neq c_K}. \tag{6}$$

L_{ij}^{K} are phenomenological chemical mobilities, calculated as the volume-average chemical mobilities inside different phases, ${}^{\alpha}L_{ij}^{K}$, (see details in [13]).

One should notice that the composition fields, $c_i(\tilde{\boldsymbol{\mu}})$, in Eq. (5) are implicit functions of the diffusion potentials, $\tilde{\boldsymbol{\mu}}$. Therefore, the solution of the mass conservation law, Eq. (5), requires the inversion of the chemical potential relation in order to express compositions $c_i := c_i(\tilde{\boldsymbol{\mu}})$ for $i = 1, \dots, K-1$. A numerical approach to achieve this chemical-potential inversion, applicable to a substitutional phase, has been recently proposed by the current authors [13,31]. In the following section, we will extend this algorithm to deal with ordered phases with two-sublattice structures, based on the semi-implicit inversion method, in the chemical-potential-based solute transport equation.

2.2.1. Two-sublattice CALPHAD model

Many ordered phases can be described by the two-sublattice model as $(\mathrm{A, B, C, ...})_{\alpha'}(\mathrm{A, B, C, ...})_{\alpha''}$, where α^{i} is the stoichiometry of each sublattice such that $\sum_i \alpha^i = 1$. For the current application to the η-phase in Al-Zn-Mg-Cu alloys, all the solute elements were allowed to occupy both the first and second sublattice. The Gibbs energy of the crystalline phase with two sublattices can be

expressed as:

$$\Omega f^{\phi}_{\text{chem}}(y_i^{(s)}) = \sum_{i=1}^{K}\sum_{j=1}^{K}\left[y_i^{'}y_j^{''}G^{\phi}_{i:j}\right] + RT\left[a^{'}\sum_{i=1}^{K}y_i^{'}ln(y_i^{'}) + a^{''}\sum_{j=1}^{K}y_j^{''}ln(y_j^{''})\right] + {}^{\text{XS}}G^{\phi}_{\text{chem}}, \quad (7)$$

where Ω is the molar volume, and $y_i^{'}$ and $y_i^{''}$ are the site fractions for component i on the first and second sublattice, respectively. The relation between the site fraction and mole fraction of component m is given by:

$$c_m^{\phi} = \frac{\sum_t a^t y_m^t}{\sum_t \sum_i a^t y_i^t}. \quad (8)$$

$G^{\phi}_{i:j}$ in Eq. (7) represents the molar Gibbs energy of the end-member compound $i_{a'}j_{a''}$. The logarithm terms in Eq. (7) express the contribution of the ideal mixing entropy. The excess term, ${}^{\text{XS}}G^{\phi}_{\text{chem}}$, describes the non-ideal interactions between elements in the phase, and is given by the Redlich-Kister polynomial (see details in Section S.3 in the supplementary material).

Assuming a system in internal equilibrium, the phase diffusion potential defined by Eq. (6) must have the same value as the diffusion potential in each sublattice [54]. Otherwise, there would be a driving force for an exchange of atoms between different sublattices. Thus, the following equal diffusion potential condition in the two-sublattice model can be obtained:

$$\tilde{\mu}_i = \tilde{\mu}_i^t \quad = \mu_i^t - \mu_K^t, \quad (9)$$

where μ_i^t and $\tilde{\mu}_i^t$ are the chemical potential and diffusion potential of component i in the t sublattice, respectively.

Following the derivation of partial quantities [54], the chemical potential of component m in the first sublattice can be calculated from the Gibbs free energy definition in Eq. (7):

$$\mu_m^{'} \quad = \Omega f^{\phi}_{\text{chem}} + \frac{1}{a^{'}}\left[\left(\frac{\partial \Omega f^{\phi}_{\text{chem}}}{\partial y_m^{'}}\right)_{y_l^{'}} - \sum_{i=1}^{K} y_i^{'}\left(\frac{\partial \Omega f^{\phi}_{\text{chem}}}{\partial y_i^{'}}\right)_{y_l^{'}}\right]. \quad (10)$$

The diffusion potential for component m in the first sublattice (Eq. (9)) can then be expressed as:

$$\tilde{\mu}_m^{'} = \frac{1}{a^{'}}\left[\frac{\partial f^{\phi}_{\text{chem}}}{\partial y_m^{'}} - \frac{\partial f^{\phi}_{\text{chem}}}{\partial y_K^{'}}\right] = \frac{1}{a^{'}}\left[\sum_{j=1}^{K} y_j^{''}G_{m:j} - \sum_{j=1}^{K} y_j^{''}G_{K:j} + RTa^{'}ln\left(\frac{y_m^{'}}{y_K^{'}}\right) + \frac{\partial {}^{\text{XS}}G^{\phi}_{\text{chem}}}{\partial y_m^{'}} - \frac{\partial {}^{\text{XS}}G^{\phi}_{\text{chem}}}{\partial y_K^{'}}\right]. \quad (11)$$

Solving the diffusion equations (Eq. (5)) as a function of the diffusion potentials requires the inversion of the diffusion potentials (Eq. (11)) in order to express $c_i := c_i(\tilde{\boldsymbol{\mu}})$ for $i = 1, \ldots, K-1$. This is achieved algorithmically, with a time-discrete approach, through a semi-implicit splitting of the diffusion potential relation in a certain sublattice:

$$\tilde{\mu}_i(t_n) = \tilde{\mu}_i^{'}(t_n) = \breve{\tilde{\mu}}_i^{'}(t_n) + \hat{\tilde{\mu}}_i^{'}(t_{n-1}), \quad (12)$$

into a convex contribution:

$$\breve{\tilde{\mu}}_i^{'}(t_n) = \frac{1}{a^{'}}\left[\sum_{j=1}^{K} y_j^{''}(t_n)G_{m:j} - \sum_{j=1}^{K} y_j^{''}(t_n)G_{K:j} + RTa^{'}ln\left(\frac{y_m^{'}(t_n)}{y_K^{'}(t_n)}\right)\right], \quad (13)$$

and a non-convex contribution:

$$\hat{\tilde{\mu}}_i^{'}(t_{n-1}) = \frac{1}{a^{'}}\left[\frac{\partial {}^{\text{XS}}G^{\phi}_{\text{chem}}}{\partial y_m^{'}}(t_{n-1}) - \frac{\partial {}^{\text{XS}}G^{\phi}_{\text{chem}}}{\partial y_K^{'}}(t_{n-1})\right], \quad (14)$$

where t_n and t_{n-1} are consecutive discrete time intervals, and local equilibrium is assumed (Eq. (9)). Based on this semi-implicit splitting approach, the site fractions in the first sublattice, $y_i^{'}$, can then be calculated in terms of diffusion potentials by the inversion of Eq. (12);

$$y_m^{'}(t_n) = \frac{\exp\left[\frac{\lambda_m^{'}(t_n) - \hat{\tilde{\mu}}_m^{'}(t_{n-1})}{RT}\right]}{1 + \sum_n^{M-1}\exp\left[\frac{\lambda_n^{'}(t_n) - \hat{\tilde{\mu}}_n^{'}(t_{n-1})}{RT}\right]}, \quad (15)$$

where

$$\lambda_m^{'}(t_n) = \tilde{\mu}_m(t_n) - \frac{1}{a^{'}}\left(\sum_{j=1}^{K} y_j^{''}(t_n)G_{m:j} - \sum_{j=1}^{K} y_j^{''}(t_n)G_{K:j}\right). \quad (16)$$

Following the above derivation, the site fractions in the second sublattice, $y_i^{''}$, can also be obtained. Eq. (15) is an implicit system of equations that can be numerically solved for a given diffusion potential, $\tilde{\boldsymbol{\mu}}(t_n)$.

2.3. Numerical implementation

The inverted thermodynamic relation for the two-sublattice phase is given by Eq. (15) for the first sublattice. The corresponding relation for the second sublattice is analogues to Eq. (15). Details of the corresponding relation for the disordered matrix phase are outlined in a previous work [13]. Substituting the above inverted thermodynamic relation, through Eqs. (1) and (8), into Eq. (5) yields the final transport equations. Together with Eq. (4), these form the governing equations to be solved as a function of solute diffusion potentials, $\tilde{\mu}_i$, and phase-field order parameters, φ^{α}. The proposed CALPHAD/phase-field model for the multi-component and two-sublattice phase has been implemented in the freeware material simulation kit, DAMASK [55], and a large-scale parallel finite element solver using the PETSc numerical library [56] has been developed to deal with the discretization and numerical solution of the coupled differential field equations. The solution approach involves solving the coupled system of Eqs. (5) and (4) within a staggered iterative loop until a self consistent solution is achieved for a time increment. The numerical solution procedure is described in detail in [31].

3. Application to η-phase precipitation in Al-Zn-Mg-Cu alloys

3.1. Experimental methods

To validate the CALPHAD parameters for the chemical free energies, available from the open source thermodynamic databases for the two sublattice η-phase [57,58], CALPHAD predictions were compared to experimentally measured equilibrium η-phase compositions. However, since the η-phase in 7xxx alloys typically exists as nanoscale precipitates, their compositions are challenging to analyse using conventional electron microscopy due to the relatively large electron-interaction volumes overlapping with the matrix phase [21]. In order to overcome this limitation, in this work, samples of interest from the T/4 plate position of five different 7xxx alloys (AA7085, AA7050, AA7040, AA7449, and AA7010) were instead solution treated at 470 °C for 1 h to dissolve all intermetallic phases present. The samples were then slowly cooled at a rate of 10K h^{-1} to promote the nucleation of large precipitates at the grain boundaries, and subsequently aged at a variety of lower temperatures for 1 week, which is sufficiently long to achieve equilibrium. By design, this heat treatment resulted in microstructures with coarse, micron-scale precipitates (an example is given in Fig. 1(a)), which were much larger than the electron interaction volumes typically used in electron microscopy with Al

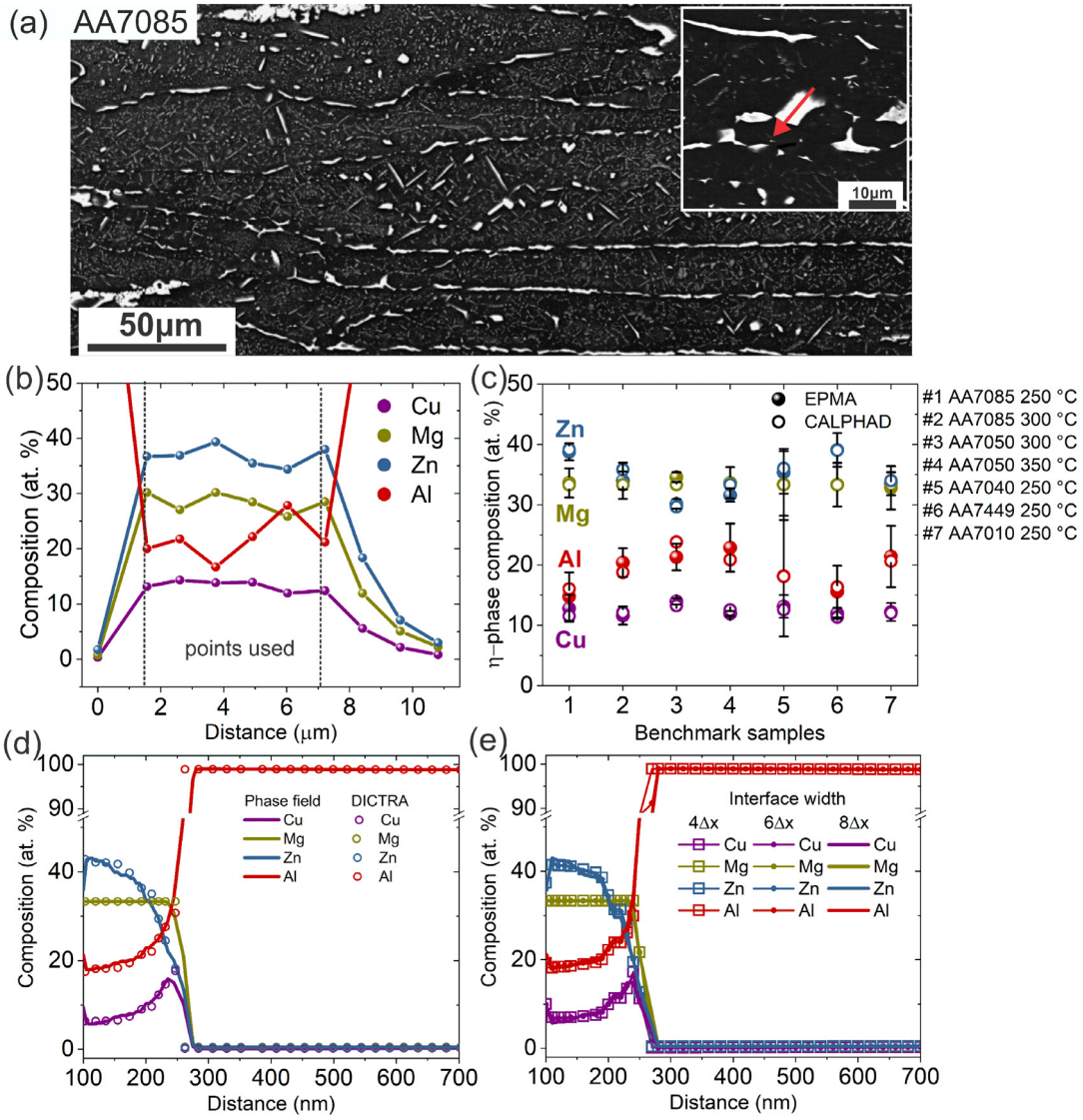

Fig. 1. Validation of the thermodynamic description of the η-phase and the phase-field model in Al-Zn-Mg-Cu systems: (a) backscatter electron micrograph of the AA7085 alloy microstructure after solution treatment, slow cooling, and long-term ageing; (b) representative EPMA line scans of a η-phase precipitate and surrounding matrix in the AA7085 alloy, along the red arrow as indicated in (a); (c) the η-phase equilibrium compositions in five different 7xxx alloys at 250 °C, 300 °C, and 350 °C, obtained from EPMA characterizations (solid circles) compared to CALPHAD predictions (open circles). The standard deviation error calculated from multiple EPMA measurements for each alloy is also included; (d) the simulated Cu, Mg, Zn, and Al concentration profiles of the η-phase in a model AA7050 alloy aged at 250 °C after 139 h. Phase-field predictions and DICTRA calculations are described by the solid lines and round symbols, respectively; (e) the corresponding phase-field simulation results with different interface widths varying from $4\Delta x$ to $8\Delta x$. . (For interpretation of the references to colour in this figure legend, the reader is referred to the web version of this article.)

[21], and their compositions were thus much more reliably analysed. The compositions of precipitates were analysed using a JEOL JXA-8530F Field Emission Gun Electron Probe Microanalyser (FEG-EPMA) equipped with 4 wave dispersive spectrometers (WDS), operated at a current of 108nA and an accelerating voltage of 15kV. Counts for Mg ($K\alpha_1$) were collected on a TAP diffraction crystal, and copper ($K\alpha_1$) and Zn ($K\alpha_1$) were collected on a LiFL diffraction crystal. To provide further confidence in the EPMA analysis of the precipitates, line scans were utilised instead of individual point analyses so that a one-dimensional composition profile of the precipitates and surrounding matrix was first collected, so that only points in the 'steady-state' central region of the precipitate were included in the results. Line scans were conducted using a dwell time of 2 min for each point with a spacing of 1 μm. An example of this approach is shown in Fig. 1(a) and (b) for AA7085, where the insert in Fig. 1(a) shows a backscatter electron micrograph of the precipitate analysed, and Fig. 1(b) shows the line scan data and the central points selected and averaged to obtain the phase composition result. Each EPMA point was collected with a single standard deviation error measurement (approx. 0.15 at.%), which were compounded during averaging.

Figure 1 (c) shows the measured equilibrium compositions of the η-phase in the different alloys at 250 °C, 300 °C, and 350 °C, respectively. The standard deviation error calculated from multiple EPMA measurements for each alloy is also included in Fig. 1(c), *i.e.* approx. 1.3 at.%, 3.5 at.%, 2.1 at.%, and 5 at.% for Cu, Mg, Zn, and Al, respectively. It is worth noting that, in order to reasonably fit the experimental measurements, re-assessment has been performed for the interaction parameter between Al and Zn in the first sublattice when the second sublattice is completely occupied by Mg. The other thermodynamic parameters are the same as in the COST507 database [57]. It can be seen that the CALPHAD calculated results (open circles) compared favourably with the experimentally measured compositions (solid circles). It is apparent that

the predicted Mg concentration of the η-phase was around 33 at.% in all cases, whereas the Cu, Zn, and Al solute concentrations in the precipitate depended on both the alloy compositions and annealing temperatures. This good agreement between the CALPHAD predictions and EPMA results thereby provides validation of the thermodynamic description of the multi-component η-phase with a two-sublattice structure.

3.2. Model validation

The validated thermodynamic parameters were directly used in Eq. (7) without any approximations or simplification. The kinetic parameters, required to calculate the solute diffusion mobilities in the disordered matrix phase, were directly obtained from the open source MatCalc solute mobility database [58]. The thermodynamic and kinetic material parameters used in the present work are summarised in the supplementary material.

In order to validate the thermodynamic driving forces and interface kinetics in the phase-field model, the growth of the η-phase in a quaternary Al-2.69 at.% Zn-2.68 at.% Mg-1.03 at.% Cu alloy at 250 °C was benchmarked with the predictions from the DICTRA sharp interface model [22]. To obtain a quantitative comparison, DICTRA simulations were also performed using the above thermodynamic and kinetic material parameters, through a user-defined database in Thermo-Calc. In this benchmark simulation, an initial η-phase composition of $(Zn_{41.1}, Al_{15.3}, Cu_{10.3})Mg_{33.3}$ was used. Solute diffusion was suppressed in the η-phase. A one-dimensional domain of length $L = 260\Delta x$ was employed, and an η-phase precipitate of size $L = 10\Delta x$ was introduced at one end of the domain. A uniform grid spacing $\Delta x = 10$nm and an interface width $\eta = 4\Delta x$ was used. Figure 1(d) shows that, after ageing for 139 h at 250 °C, Cu, Mg, Zn, and Al solute profiles of the η-phase predicted by the phase-field model were in good agreement with the calculations from the sharp interface model. The small deviations in the interfacial region can be ascribed to the diffuse interface characteristic of the phase-field model. Furthermore, Fig. 1(e) shows the phase-field simulation results with various interface widths from $4\Delta x$ to $8\Delta x$. It is apparent that the simulated evolution of the precipitate composition was independent of the interface width, which benefited from the quasi-equilibrium condition [37] being implicitly satisfied in the current model. In the following simulations, an interface width of $4\Delta x$ was used to enable the simulation of the same total physical size with coarser finite element discretization and efficient numerical calculations.

3.3. Simulation setup

Following the model validation, the CALPHAD/phase-field model was used to quantitatively investigate the complex compositional pathway for the formation of η-phase, to better understand the effect of alloy compositions and ageing conditions on the compositional and microstructural evolution of the η-phase precipitates. To this end, a single crystal with multiple pre-introduced η-phase nuclei was created to serve as the starting configuration. The domain size modelled was 256nm × 256nm, with a uniform grid spacing of $\Delta x = \Delta y = 0.5$nm and an interface width of $\eta = 4\ \Delta x$. The initial radius and number density of η-phase nuclei used in the model were 3 nm and 1000 μm^{-2}, respectively, informed by the APT characterisation of an AA7050 alloy aged at 120 °C for 2 h [20]. These precipitate nuclei were randomly distributed in the matrix at the beginning of the simulation. Periodic boundary conditions were applied to the simulation domain. Since the thermodynamic description of the prior metastable GPZs and η' transition phase is still the subject of some speculation [57,59], the present work particularly focuses on the study of the compositional evolution during η-phase formation. Since reported aspect ratios of the η-precipitate in 7xxx alloys was relatively small (2 - 3) [17,20], an isotropic interface energy of 0.5Jm^{-2} was assumed for the precipitate-matrix interface (see detail in Section S.2 in the supplementary material). An interface mobility of $1 \times 10^{-11} m^4 J^{-1} s^{-1}$ was used, which is large enough to guarantee that the η-precipitate growth was a diffusion-controlled process. Constant molar volumes, $\Omega = \ 1 \times 10^{-5} m^3 mol^{-1}$, were assumed for both the solid solution phase and η-phase. To the authors' knowledge, since the kinetic parameters used to calculate the diffusivities in the ordered η-phase are not available in the published literature, the solute mobilities in the η-phase are assumed be of the same order of magnitude as in the matrix phase.

Three different model 7xxx alloys have been simulated and compared in the present work. The first alloy, AA7050 (Al - 2.69 at.% Zn - 2.68 at.% Mg - 1.03 at.% Cu), had the highest Cu and the lowest Zn concentration. The second alloy, AA7085 (Al - 3.30 at.% Zn - 1.80 at.% Mg - 0.72 at.% Cu), had the lowest Cu and the highest Zn concentration. The last alloy, AA7010 (Al - 2.76 at.% Zn - 2.79 at.% Mg - 0.76 at.% Cu), had similar Mg and Zn concentrations to AA7050, but with a lower Cu concentration. The AA7085 alloy represents a more modern generation high Zn content 7xxx alloy, while AA7050 and AA7010 are lower Zn content established industry 'workhorse' materials. It should be noted that the three alloys studied in the current work all represent model 7xxx alloys, and the influence of impurity elements on the microstructure evolution was thus not considered in the current simulations.

3.4. η-Phase precipitation in the AA7050 alloy

An isothermal ageing simulation was first performed for AA7050 at 180 °C, in order to track and quantify the complex compositional pathway for the formation of the η-phase. Figure 2 shows the simulated compositional and morphological evolution of η-phase precipitates after ageing for 0.3 h, 1.0 h, and 5.3 h. In general, both the Cu and Al content in η-phase precipitates increased progressively with ageing time, while there was a distinct reduction in the Zn content. In comparison, a constant Mg concentration of 33.3 at.% has been predicted throughout the ageing process. A closer inspection of the solute partitioning in the precipitates after 5.3 h ageing (as shown in Fig. 2(c)) reveals that all the solute elements (Cu, Zn, and Al), except for Mg, were distributed heterogeneously across precipitates. Considerably higher Cu and Al concentrations can be observed in the precipitates with smaller sizes, whereas the corresponding Zn content exhibited the opposite trend. A further quantitative study on the compositional evolution of the η-phase and the correlation between the precipitates' compositions and their size distributions will be presented below.

The evolution of the solute distribution in the matrix is provided in Fig. 3(a–c). The results indicate that the Cu depletion zone that developed at the early ageing times was restricted to a narrower layer (approx. 13nm wide at 0.3 h) adjacent to precipitates. However, both the Mg and Zn solute depletion zones have completely overlapped after an early ageing time of 0.3 h at 180 °C. Upon further ageing to 1 h, a virtually homogeneous distribution of Mg and Zn can be observed in the matrix. In comparison, Cu was found to remain significantly supersaturated and more heterogeneously distributed in the matrix. Figure 3(d) depicts the evolution of example composition profiles across the matrix and precipitates (along the black arrow as indicated in Fig. 3(c)). When ageing from 1 h to 5.3 h, the solute depletion surrounding the central smaller precipitate progressively transitioned to enrichment for all solute elements (Cu, Mg, Zn). This was accompanied by the shrinkage of this precipitate (from 4nm to 1nm), consistent with the effect of Ostwald ripening, and a significant enrichment of Cu (from 10.2

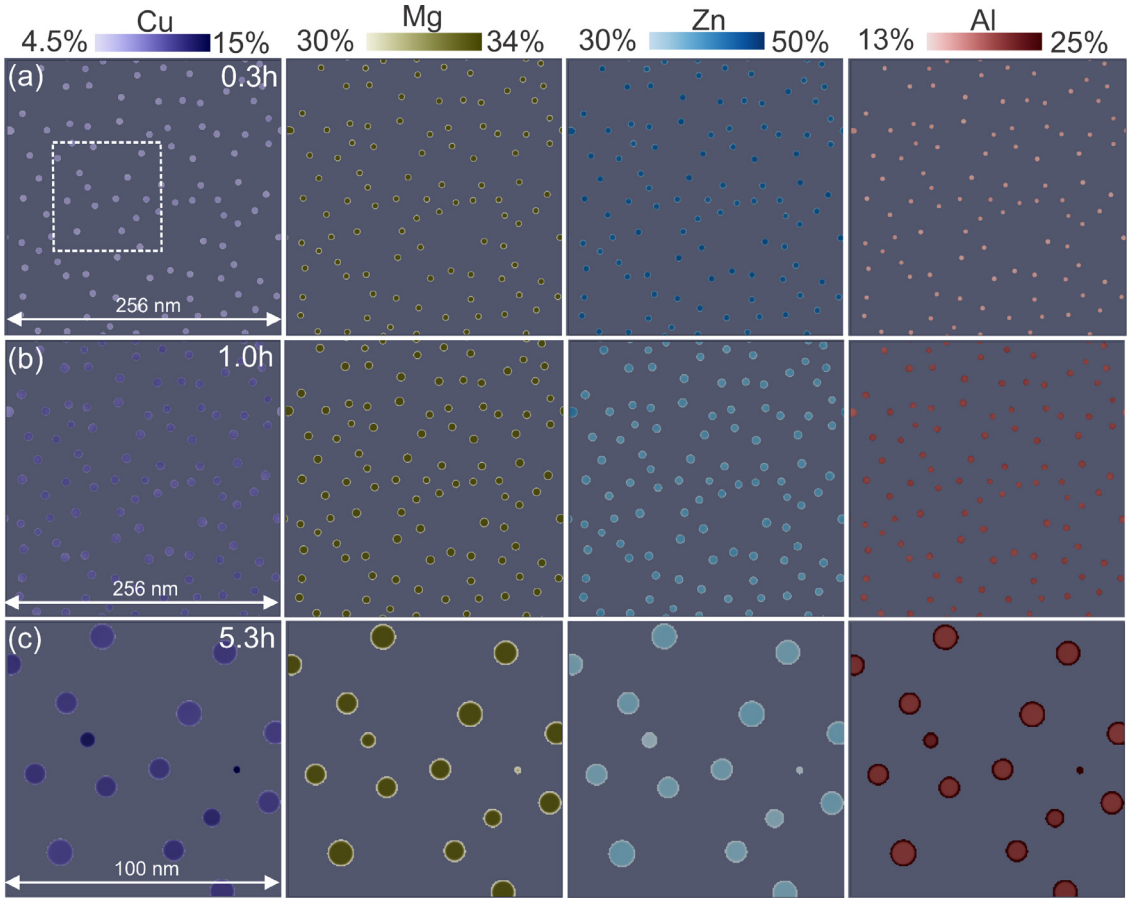

Fig. 2. Evolution of the Cu, Mg, Zn, and Al solute distributions in the η-phase precipitates at ageing times of (a) 0.3 h, (b) 1 h, and (c) 5.3 h at 180 °C in AA7050. (c) shows the enlarged simulation region as indicated by the white square in (a). The matrix solute distribution is shown below in Fig. 3.

at.% to 16.1 at.%) and depletion of Zn (from 37.2 at.% to 25.3 at.%) in the precipitate.

To quantify the compositional pathway for the formation of the η-phase, Fig. 4(a–d) and (j) track the solute composition and radius of individual precipitates during ageing at 180 °C in AA7050. All precipitates were observed to grow rapidly during the early stages of ageing (up to approx. 0.8 h). After the initial growth stage, Ostwald ripening can be observed from 1 h to 5.3 h ageing. As shown in Fig. 4(a), the Cu concentration in all the precipitates increased continuously from approximately 7 at.% to 11 at.% with increasing ageing time up to 2.5 h. Upon further increasing ageing time, clear differences in the Cu content between different precipitates developed. Comparison of Fig. 4(a) and (j) suggests that the Cu content in the smaller precipitates increased sharply to a maximum value of about 15 at.% during the Ostwald ripening process, which was accompanied by the shrinkage of these smaller precipitates until their eventual dissolution. In comparison, the corresponding Zn evolution was characterised by a substantial reduction by approx. 8 at.% (Fig. 4(c)).

As shown in Fig. 4(k–n), after 5.3 h ageing at 180 °C, a linear relationship between the precipitate compositions and the inverse of the precipitate radius can be observed, consistent with the Gibbs-Thomson effect [60]. The evolution of the matrix-interface solute composition (Fig. 4(e–g)), shows that all the solute compositions with respect to these smaller precipitates exhibited a progressive enrichment during the Ostwald ripening process. A steep increase of all the solute concentrations, especially for Cu, can be observed when the smaller precipitates approached the threshold for dissolution. Figure 4(i) further illustrates that for the smaller dissolving precipitates the Cu/Zn ratio in the interfacial matrix increased continuously with ageing time, although the mean Zn content in the precipitates was almost three time higher than for Cu. Moreover, the Cu/Zn ratio in these smaller precipitates was predicted to increase as a function of ageing time, as shown in Fig. 4(h). These observations suggest that the strong enrichment of Cu, both in the smaller precipitates and in the interfacial matrix, stems from the kinetic control of the η-phase formation; *i.e.* more Zn solute atoms with higher diffusivity compared to Cu have diffused away from the smaller precipitates to the larger ones during Ostwald ripening.

Figure 5 (a) and (b) show the evolution of the precipitate volume fraction and the average solute compositions of the precipitates and the matrix, during ageing at 180 °C in AA7050. It can be seen that the average Mg and Zn concentration exhibited a considerable reduction from 2.7 at.% to 0.5 at.% after 1 h ageing, and then remained virtually constant. In contrast, the depletion kinetics of Cu from the matrix was much slower. Although the average Zn composition in the matrix reduced to a steady state value after only 0.5 h ageing, the precipitate volume fraction increased from 7.8% to 9% with subsequent ageing to 1.5 h (as shown by the black curve in Fig. 5(a) and (b)). This is accompanied by a decrease in the average Zn concentration of the precipitates from 41 at.% to 36 at.%, while both the Cu and Al average precipitate concentration exhibited distinct enrichment, from 8 at.% to 11 at.% and from 18 at.% to 20 at.%, respectively. In Fig. 5(c) it can be observed that the average Cu/Zn ratio in the matrix increased significantly from 0.4 to 1 at early ageing times and reached a maximum value after 0.5 h, at which point the available Zn in the matrix has been

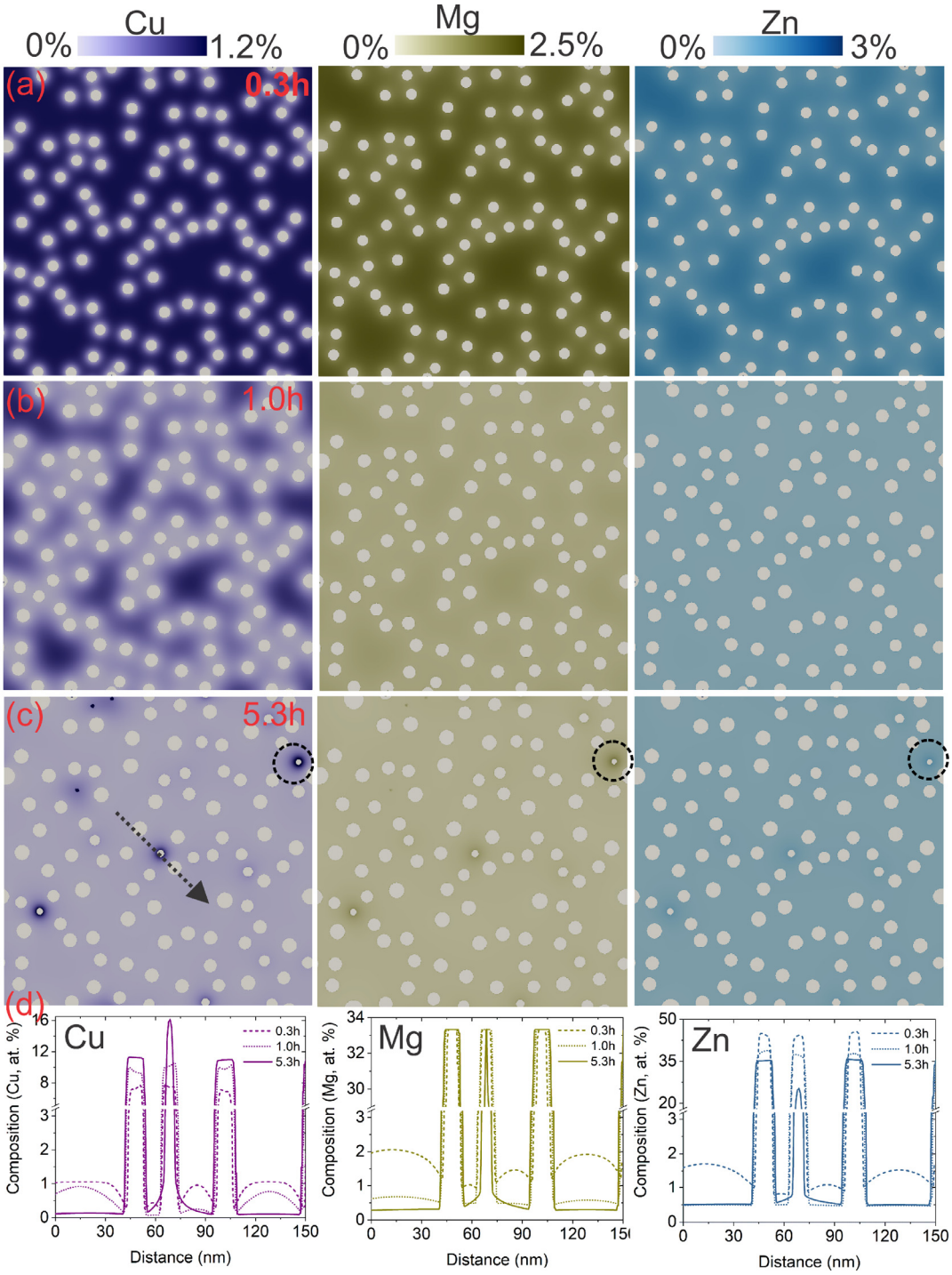

Fig. 3. Evolution of the Cu, Mg, and Zn solute distributions in the matrix at ageing times of (a) 0.3 h, (b) 1 h, and (c) 5.3 h at 180 °C in AA7050. (d) The corresponding solute composition profiles across the matrix and precipitates, along the black arrow as shown in (c).

completely consumed by precipitates. The matrix Cu/Zn ratio then gradually decreased to a steady value of 0.3 after 2.5 h ageing. These two distinct evolution trends are dominated by Zn depletion and Cu depletion in the matrix, respectively.

3.5. Influence of alloy composition

In this section the influence of alloy composition on η-phase precipitation is systematically investigated. As described in Section 3.3, three different 7xxx alloy variants (AA7050, AA7010, AA7085) have been studied and compared in the present work. Isothermal simulations were conducted at 180 °C up to 3.5 h.

Figure 6 compares the effect of alloy composition on the solute distribution in the η-phase precipitates after 3.5 h ageing at 180 °C. The Cu content in η-phase precipitates was predicted to be highest in AA7050, and lowest in AA7085. The Cu content of the precipitates in AA7010 lies in between that of the two other alloys. In contrast, the Zn composition in the η-phase precipitates exhibited the opposite trend. These observed Cu and Zn partitioning levels in the η-phase are consistent with the relative global compo-

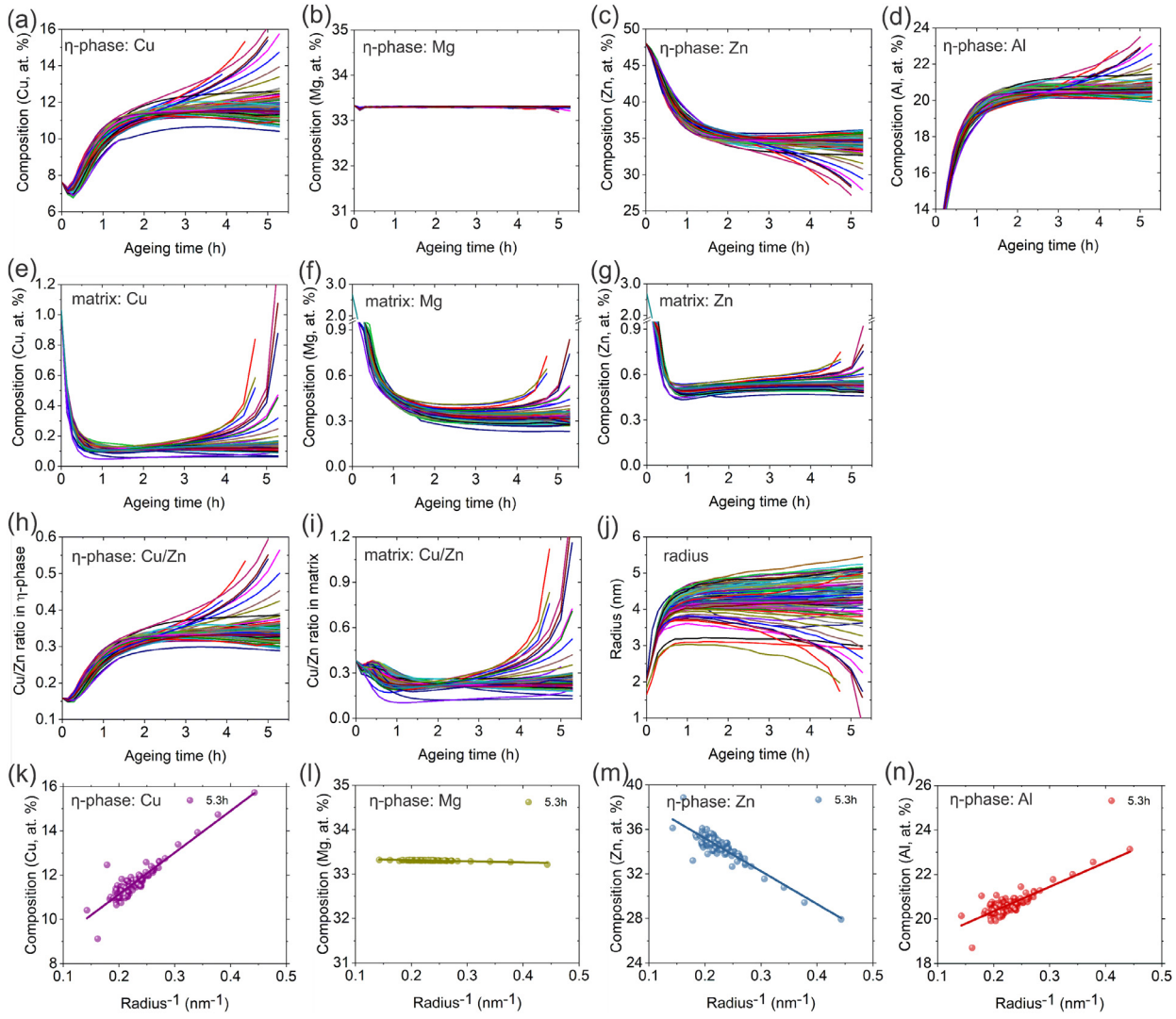

Fig. 4. Evolution of individual solute compositions over ageing time at 180 °C in AA7050, showing the (a) Cu, (b) Mg, (c) Zn, and (d) Al composition in individual precipitates and the corresponding (e) Cu, (f) Mg, and (g) Zn composition in the matrix-interface; the evolution of the ratio of Cu to Zn (h) in the precipitates and (i) in the interfacial matrix, and the radius of the individual precipitates over ageing time. Relationship between the precipitate solute composition and the inverse of the precipitate radius for (k) Cu, (l) Mg, (m) Zn, and (n) Al at an ageing of time of 5.3 h at 180 °C.

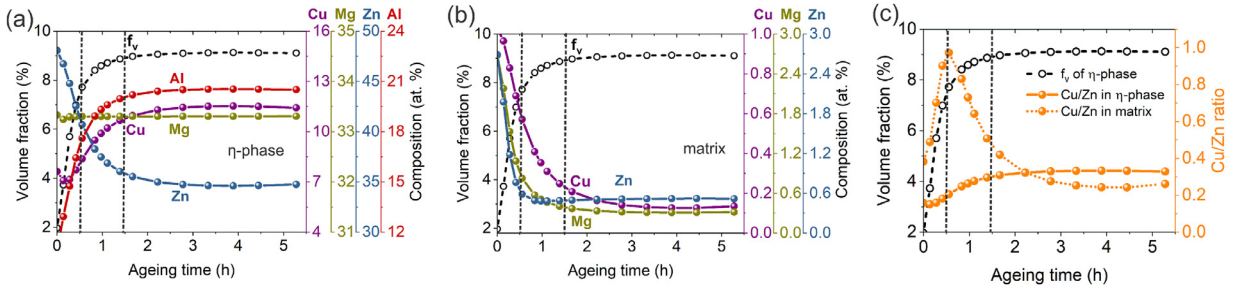

Fig. 5. Evolution of the average solute compositions of (a) the precipitates and (b) the matrix; and (c) the temporal evolution of the average Cu/Zn ratio in the precipitates and matrix, in relation to the change in the precipitate volume fraction, during ageing at 180 °C in AA7050.

sitions in Zn and Cu of the three alloys. Moreover, similar Al contents in the η-phase can be observed in both AA7050 and AA7010, whereas in AA7085 the precipitates contained a relatively low Al level.

Figure 7 (a–d) present the size-dependent compositional behaviour of the η-phase precipitates after 3.5 h ageing at 180 °C. For all the three alloys studied, both the Cu and Al content were found to linearly increase with the inverse of the precipitate radius, whilst Zn had the opposite variation. In addition, it can be seen that, for each solute element, the slopes of the size-composition correlation lines for the η-phase precipitates were almost identical for various 7xxx variants studied, though with a large relative shift. Moreover, the corresponding evolution of the matrix-interface solute compositions, against the inverse of the precipitate radius, is also provided in Fig. 7(e–g), where a linear relationship was again obtained for all the 7xxx alloys studied.

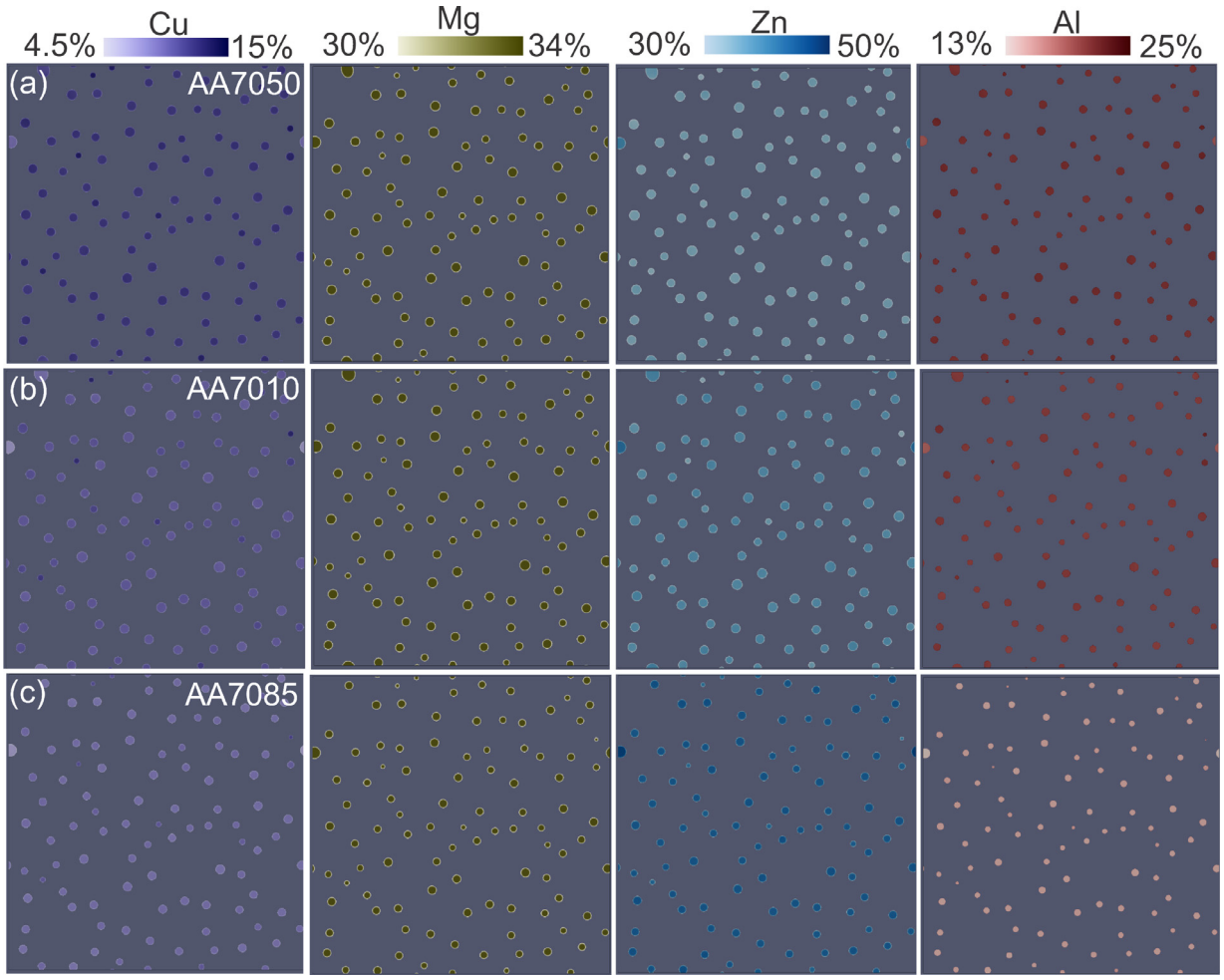

Fig. 6. Solute distributions in the η-phase precipitates in the (a) AA7050, (b) AA7010, and (c) AA7085 alloys after 3.5 h ageing at 180 °C.

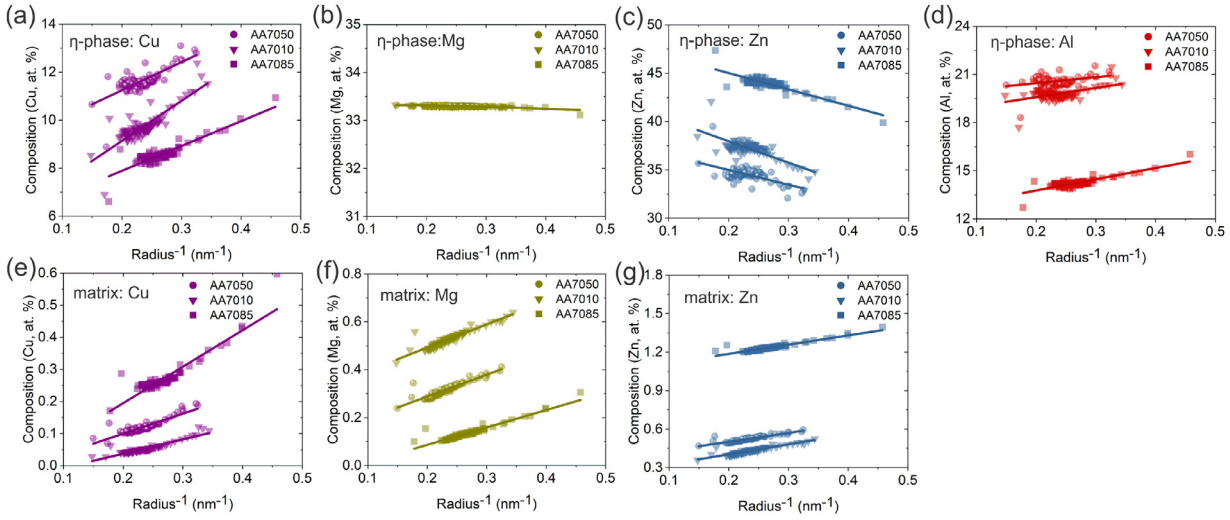

Fig. 7. Effect of alloy composition on the relationship between the solute partitioning and the precipitate size on ageing at 180 °C for 3.3 h; (a–d) solute compositions in η-phase precipitates *vs* inverse of the precipitate radius, (e–g) solute compositions in the matrix-interface *vs* inverse of the precipitate radius.

The effect of alloy compositions on the evolution of the average solute compositions in the η-phase precipitates and in the matrix with ageing time at 180 °C is illustrated in Fig. 8. After 3.5 h ageing at 180 °C, the average η-phase compositions in AA7050, AA7010, and AA7085 were predicted to be $(Zn_{34.7}, Al_{20.5}, Cu_{11.5})Mg_{33.3}$, $(Zn_{37.5}, Al_{19.7}, Cu_{9.5})Mg_{33.3}$, and $(Zn_{44.1}, Al_{14.2}, Cu_{8.4})Mg_{33.3}$, respectively. Fig. 8(a) shows that AA7050 exhibited the highest average Cu and lowest Zn content in the η-phase precipitates throughout the ageing process. With respect to the evolution of the solute contents in the matrix, as shown in Fig. 8(b), AA7085 exhibited sig-

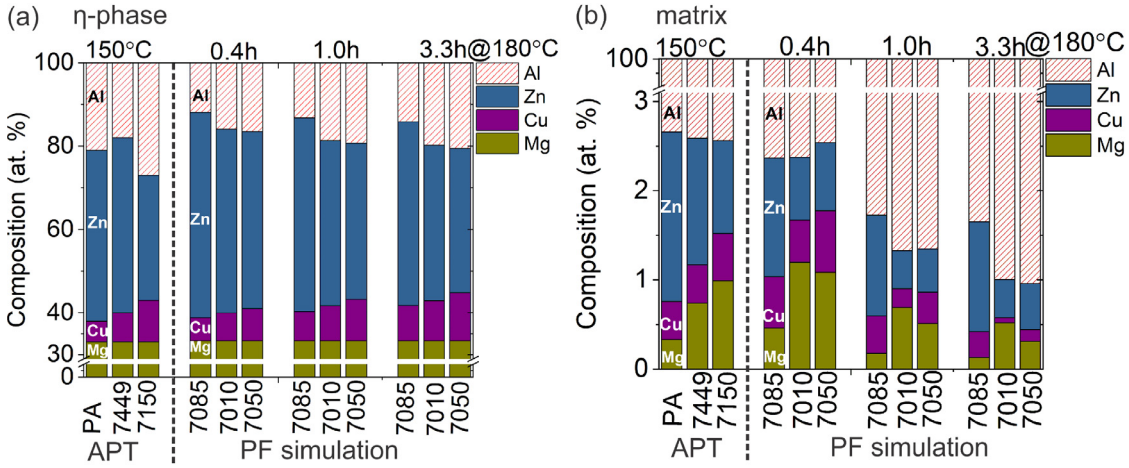

Fig. 8. Effect of alloy composition on the evolution of the average solute compositions in (a) the η-phase precipitates and in (b) the matrix as a function of ageing time at 180 °C. The corresponding experimental results at 150 °Cfrom the APT characterisations are also included [16,17].

nificantly higher Cu and Zn matrix compositions, throughout the ageing process (apart from the initial 0.7 h ageing), compared to the two other alloys. For example, ageing for 1 h at 180 °C, AA7085 had nearly three times higher residual Zn and twice the Cu content compared to AA7050 (1.1 at.% relative to 0.4 at.%, 0.4 at.% relative to 0.2 at.%, respectively). The residual Mg content in the matrix was, however, lowest for AA7085 across the entire ageing time.

3.6. Influence of ageing temperatures

It is widely acknowledged that the SCC resistance in 7xxx alloys can be markedly improved by tuning the composition of η-phase precipitates and the corresponding residual solid solution, through for example, retrogression and re-ageing treatments [17,61–67], or two-step overageing heat treatments [16,68–72]. Understanding the influence of ageing temperatures on the evolution of the η-phase composition is, thus, a key avenue for advancing the development of 7xxx alloys. In this section, a two-step ageing simulation was first conducted for AA7050. The alloy was initially heat treated at 120 °C for 24 h, and then subjected to an overageing treatment at 180 °C for 2.5 h, at a heating rate of 60°Cs^{-1}. Furthermore, three additional isothermal ageing simulations have been investigated for AA7050 at 120 °CC, 180 °C, and 250 °C, respectively.

Figure 9 (a) and (b) depict the simulated solute distribution in the η-phase precipitates for AA7050 during the two-step ageing process. It can be seen that, in comparison to the ageing state after the first ageing step (Fig. 9(a)), both the Cu and Al concentrations in the precipitates exhibited a significant increase, after only 25 min at 180 °C (Fig. 9(b)), whilst a sharp reduction in Zn was predicted. In addition, Fig. 9(c) shows that, after 24 h ageing at 120 °C, both Mg and Zn are distributed heterogeneously in the matrix, while in contrast, a more homogeneous distribution of Cu can be observed with a markedly narrower Cu depletion zone near the precipitates. However, when the alloy was subsequently subjected to ageing at 180 °C for 25 min, both Mg and Zn rapidly became homogeneously distributed in the matrix and no obvious solute depletion zones can be found. In contrast, the distribution of Cu was still relatively heterogeneous, and the depletion zones have started to overlap.

As shown in Fig. 10(a), with increasing from 6 h to 24 h at 120 °C, the precipitate volume fraction was found to gradually increase from 5% to 8%. Over the same time-scale, only a 0.7 at.% Cu increase in precipitates was predicted, while the Zn content exhibited a relatively large reduction by almost 4 at.%. After 1 h ageing at 180 °C, the precipitates continued to become richer in Cu and Al by 4 at.% and 2.5 at.%, respectively, compared to a significant depletion in Zn. With respect to the evolution of the solute concentrations in the matrix, shown in Fig. 10(b), after increasing the ageing temperature to 180 °C the matrix Zn concentration remained nearly constant. This indicates that the available Zn solute in the matrix was completely consumed by η-phase growth in the first ageing step, but then readjusted as the precipitates dissolved slightly on increasing the ageing temperature. In comparison to Zn, Cu exhibited a continuous reduction in the matrix during the second ageing stage. Overall, during the second step ageing, this pronounced enrichment of Cu in the precipitates was accompanied by a rapid depletion of Cu in the matrix, while the residual matrix Zn content remained stable. This reveals that the enrichment of Cu in the η-phase at high temperature arises from both the thermodynamic factor (*i.e.* the higher supersaturation of Cu relative to Zn, which is near equilibrium in the matrix), and the kinetic control (*i.e.* two orders of magnitude higher Cu diffusivity at 180 °C compared to 120 °C).

Figure 11 (a) further shows the influence of isothermal ageing temperatures on the equilibrium η-phase compositions in AA7050, based on the CALPHAD calculations. When increasing from 120 °C to 250 °C, the calculated equilibrium Cu and Al concentration in the η-phase showed slight increases of 1 at.% and 2.5 at.%, respectively, compared to a moderate 3.5 at.% reduction in Zn. This suggests that, from the thermodynamic perspective, the ageing temperate (in the range of 250 °C) plays a minor role in the determination of the equilibrium η-phase composition. In comparison Fig. 11(e–h) show the kinetic evolution of the η-phase compositions with ageing time at 120 °C, 180 °C, and 250 °C, predicted by the phase-field model. The growth of η-phase precipitates was predicted to exhibit significantly different compositional pathways as a function of the ageing temperature, particular with regard to their Cu content. At 250 °C, a relatively high Cu concentration of 11 at.% in the η-phase has already been achieved at the beginning of ageing (6 min). In contrast, at 180 °C, the average Cu content was predicted to increase progressively from approx. 7 at.% to 11.5 at.% with increasing ageing times up to 2.5 h. Finally, at the lowest temperature of 120 °C, the average η-phase Cu content (which started at 7 at.%) was predicted to take up to 20 h before it started to increase, while the corresponding Zn and Al concentration exhibited a moderate rate of depletion and enrichment than seen on ageing at higher temperatures. Figure 11(b) and (d) show that the equilibrium matrix Zn concentration was almost achieved after ageing for 20 h at 120 °C, while Cu was still supersaturated even after 120 h ageing.

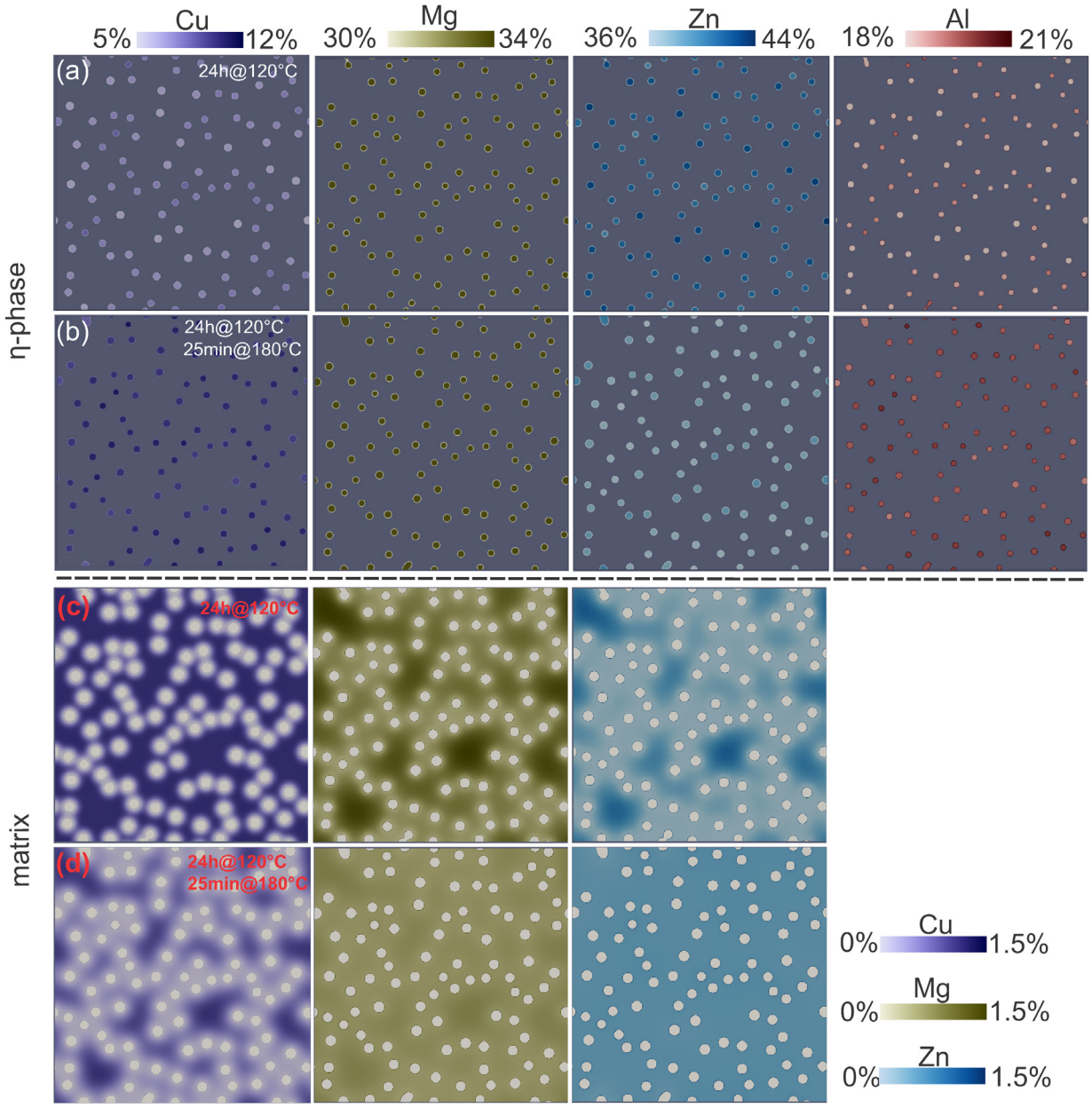

Fig. 9. Solute distributions in (a, b) the η-phase precipitates and in (c, d) the matrix during the two-step ageing simulation in AA7050: (a, c) after the first ageing step at 120 °C for 24 h, (b, d) after only for 25 min of the second ageing step at 180 °C.

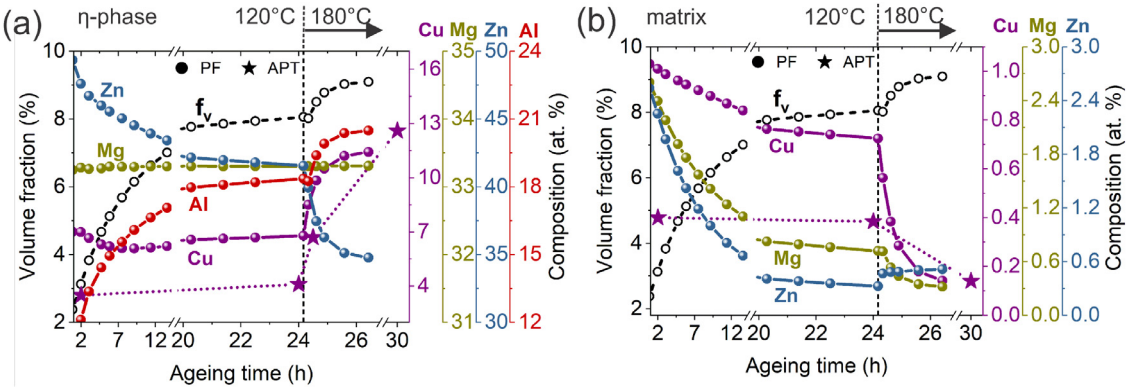

Fig. 10. Evolution of the precipitate volume fraction and the average solute compositions of; (a) the η-phase precipitates and (b) the matrix in AA7050 during the two-step ageing simulation, involving 24 h ageing at 120 °C, followed by 2.5 h at 180 °C. The star symbols show the evolution of the Cu composition in the (a) η-phase and (b) matrix of the same model AA7050 alloy characterised by APT experiments [20,73].

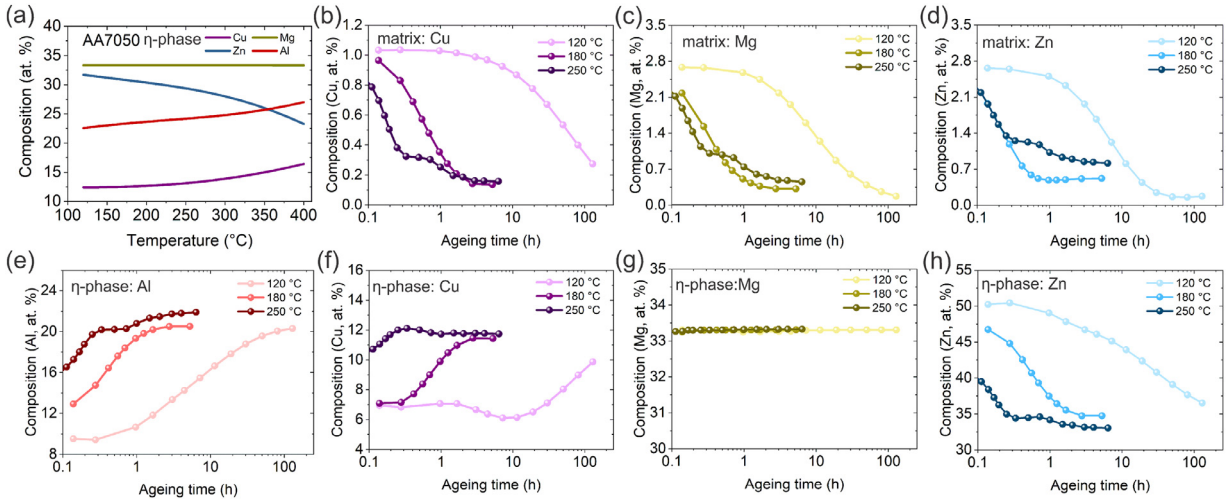

Fig. 11. Effect of ageing temperatures on (a) the equilibrium η-phase compositions calculated by the CALPHAD method; and the temporal evolution of the average solute compositions in (b–d) the matrix, and (e–h) η-phase precipitates in AA7050, predicted by the phase-field model.

4. Discussion

Although a fine distribution of GP zones and η' precipitates primarily contributes to the superior strength of Al-Zn-Mg-Cu alloys at the peak aged temper [3–12], overageing with controlled heating rates and two or more isothermal stages is usually employed to achieve the best balance of mechanical and electrochemical properties [15–17,61–72,74]. It is well recognised that η-phase transformation dominates the precipitation process in the overaged state [10]. Furthermore, direct heterogeneous nucleation and subsequent growth of the η-phase predominantly occurs along grain boundaries during quenching and early stage ageing [21], where their corrosion behaviour is very important in this alloy series. Therefore, in addition to the sizes and spatial distribution of the η-phase precipitates, it is highly desirable to be able to predict the chemical composition of the precipitates to optimize the required in-service performance of 7xxx alloys. The phase-field model developed has thus been designed so that it can more accurately represent the solute solution phase and η-phase as substitutional and two-sublattice structures, respectively. Moreover, it has been demonstrated that the required chemical free energies and solute activation energies can be directly incorporated from well-established CALPHAD thermodynamic and kinetic databases. Therefore, this representation has the key advantage that it makes it possible to simulate the η-phase precipitation process in different 7xxx alloys at various ageing temperatures; and thereby provide quantitative insight into understanding the complex compositional pathways for the formation of the η-phase.

4.1. Comparison and assessment of the simulations and experimental results

The composition of the nanoscale η-phase is typically challenging to characterise using either conventional electron microscopy, owing to the relatively large electron-interaction volumes overlapping with the Al matrix [21], or APT techniques, due to the poor sampling statistics [3,16,17,20,73,75,76]. Furthermore, the η-phase precipitates are not necessarily at equilibrium, and their composition evolves during artificial ageing treatments, depending on both the alloy composition and thermal path [16,17,20,21,73], as has been demonstrated in Figs. 8, 10 and 11. Although a large scatter of the η-phase composition measured by different characterisation technologies (as summarised in Table S1 in the supplementary material) has been reported [3,16,17,20,21,73,75,76], the experimental results clearly show that Cu and Zn in the η-phase exhibit distinct enrichment and depletion, respectively, with increasing the ageing temperature. And Cu and Zn partitioning levels in the η-phase are consistent with the relative global solute compositions of Cu and Zn in the alloy. While some simplifications have been introduced in the current model, *e.g.* non-incorporation of the prior metastable GPZs and η' transition phase, simplification of the interface energy and misfit strain, the phase-field simulations were able to predict these general trends, as shown in Sections 3.4, 3.5, 3.6.

Given the deviations of the experimental measurements and the model simplifications, some qualitative comparisons have been performed to assess and justify the current phase-field predictions. In Fig. 10, the simulated evolution of the Cu concentration in both the η-phase precipitates and the matrix phase for AA7050 was compared with the corresponding APT characterisations on the same model alloy [20,73]. It is worth noting that the Cu concentration in the grain boundary η-phase precipitates instead of bulk precipitates from the APT experiments was used for comparison, since η'-phase precipitates were usually observed in the matrix at the low ageing temperature of 120 °C, which were not considered in the current simulations. As shown in Fig. 10(a), an approximately constant η-phase Cu concentration can be observed in both the simulations (around 7 at.%) and experiments (around 4 at.%) throughout the first 24 h ageing stage at 120 °C. After the subsequent 20 min ageing at 180 °C, a sharp increase of the η-phase Cu concentration has been revealed by both the simulations (from approx. 7 at.% to 10 at.%) and experiments (from approx. 4 at.% to 7 at.%). After long time overaging at 180 °C, the predicted η-phase Cu concentration (approx. 11.5 at.% after 2.5 h) was found to be close to the experimental measurement (approx. 12.6 at.% after 6 h). With respect to the matrix Cu composition evolution, both simulations and experiments exhibited a similar characteristic, *i.e.* a slight matrix Cu depletion was observed within the first ageing step, which was followed by a sharp decrease when increasing the ageing temperature to 180 °C.

The phase-field predicted compositional evolution of the η-phase and the matrix phase in different alloys (AA7050, AA7010, AA7085) was also compared with the results from the combined APT and anomalous X-ray small-angle scattering (ASAXS) experiments on AA7150, AA7449, and PA alloys [16,17], as shown in Fig. 8. AA7085 and PA alloys are modern generation higher Zn content 7xxx alloys in the simulations and experiments, respectively, while AA7050 and AA7150 alloys represent the lower Zn content materials. The experimental characterisation [16,17] indicated that

the precipitate Cu concentration was relatively low (approx. 2 at.%) after ageing of 22 h at 120 °C and was alloy independent. When increasing the ageing temperature to 150 °C, a significant Cu enrichment in precipitates was observed for all the three alloys, *i.e.* from approx. 2 at.% to 10 at.%, 7 at.%, and 5 at.%, respectively. And the precipitate Cu concentration strongly depended on the alloy Cu content. Again, as shown in Figs. 8(a) and 10(a), the general trend of the alloy composition and ageing temperature dependent Cu concentration in the η-phase predicted by the phase-field model agrees well with the experimental characterisations. In addition to the precipitate compositions, the residual matrix composition of the three alloys measured by the APT characterisations [16,17] was also compared with the phase-field predictions (Fig. 8(b)). Since the ageing temperatures performed by the experiments and simulations were different, the experimental ageing process of 22 h at 120 °C and 8h at 150 °C was chosen to qualitatively compare with that of 0.4 h at 180 °C in the simulations. For these two processes, the overall residual matrix composition was on the similar magnitude (around 2.5 at.%). As compared in Fig. 8(b), both simulations and experiments show that although the total residual matrix composition and the residual Cu content were approximately alloy independent, the highest residual Zn concentration was found in the AA7085 and PA alloys, corresponding to the global alloy compositions.

4.2. Compositional pathways for the formation of the η-phase

The simulated compositional evolution of the η-phase in all the three alloys (AA7050, AA7010, AA7085) at 180 °C was characterised by the more gradual enrichment of both Cu and Al in the η-phase during the ageing process, accompanied by progressive Zn depletion. The same trends were also seen at all simulated ageing temperatures, however the relative rates of diffusion meant that equilibrium would be hardly achieved within a commercial heat treatment at low temperatures (*e.g.* 120 °C), and the compositions approached equilibrium much more quickly at higher temperatures. The simultaneous enrichment of Cu and Al elements in the η-phase can be partly attributed to the opposite effects of Al and Cu substitution on the lattice parameter of the η-phase [77], and the thermodynamic stabilization of the crystal structure [59].

Owing to the intrinsic two-sublattice characteristic of the η-phase (C14 Laves phase) and the distinctly different diffusivities of solute species, the compositional pathway for formation of the η-phase is also expected to be significantly influenced by the multicomponent diffusion kinetics. For example, based on the CALPHAD kinetic database [58], the self-diffusion mobilities for Zn is almost 40 times higher than for Cu in the AA7050 alloy at 180 °C. Moreover, the cross-mobilities for Cu (L^{FCC}_{CuMg} and L^{FCC}_{CuZn}) are approximately of the same order of magnitude compared to their self-mobility (L^{FCC}_{CuCu}). The large negative cross-mobilities of Cu imply that Cu transport is also substantially affected by uphill diffusion along gradients in the Mg and Zn composition. The influx of Mg and Zn solutes from the far-field matrix into the solute depletion zones near the growing precipitates would thus lead to an outflux of Cu to the neighbouring matrix. Therefore, the slower diffusivity of Cu and its outflux transport arising from the more rapid Zn and Mg influxes results first in the considerable enrichment of Zn in the η-phase at the beginning of ageing, and the subsequent incorporation of Cu, which occurs predominately only after the available Zn solute in the matrix has been completely consumed. For example, as shown in Fig. 5, after only 0.5 h ageing at 180 °C, the residual Zn in the matrix has been depleted to a stable level, while the Cu in the matrix was still highly supersaturated. When increasing the ageing time from 0.5 h to 1.5 h, continuous Cu enrichment in the η-phase and corresponding Cu depletion in the matrix can be observed, whereas the Zn concentration in the matrix remained stable. In addition, an almost linear η-phase growth kinetic relation has been predicted during the early ageing stage, until the residual Zn in the matrix reduced to a stable level after 0.5 h at 180 °C, after which the η-phase growth rate exhibited a more gradual decrease. Comparison between the predicted matrix solute composition evolution and η-phase growth kinetics, implies that Zn exhaustion mainly controlled the precipitate growth process in the early stage of ageing, leading to initial fast η-phase growth kinetics, enrichment of Zn in the η-phase, and an excess in residual Cu in the matrix. However, when the available matrix Zn atoms have been completely consumed, the diminished η-phase formation driving force was then be primarily contributed by the supersaturated Cu solute in the matrix; *i.e.* the later stage of η-phase growth was dominated by the relatively slower diffusion of Cu atoms into the precipitates, which is accompanied by Cu and Al enrichment displacing the Zn. The simulation has thus confirmed that the gradual substitution of Cu for Zn sites in the η-phase during ageing is essentially the kinetically controlled process in the later stage of ageing, due to the slower diffusivity of Cu compared to Zn in the Al matrix [13,16,17,21].

4.3. Alloy composition and ageing temperature: coupled thermodynamic and kinetic analysis

Understanding the role of alloy composition on the thermodynamics and kinetics of the formation of the η-phase is important for tuning the composition of precipitates, since both the chemical free energy and solute mobility activation energy are composition dependent. As calculated from the CALPHAD thermodynamic and kinetic databases [57,58], the ratio of self-mobilities of Cu, Mg, and Zn species in AA7050 to those in AA7085 at 180 °C is $L^{7050}_{CuCu}/L^{7085}_{CuCu} \approx 2.2$, $L^{7050}_{MgMg}/L^{7085}_{MgMg} \approx 1.7$, and $L^{7050}_{ZnZn}/L^{7085}_{ZnZn} \approx 0.9$, respectively. This suggests that although the diffusivities of the solute elements are composition dependent, they are still of a similar order of magnitude in the different 7xxx alloys. Moreover, the simulated compositional evolution of the η-phase and matrix in the different alloys during ageing exhibited a similar trend, though with a large shift between them. This implies that alloy composition plays only a minor role in the kinetics of the η-phase formation.

The distinctly different solute partitioning behaviour in the η-phase precipitates and the matrix at 180 °Cin the 7xxx alloys studied, both during the formation process and at the equilibrium state, can thus be largely attributed to the influence of alloy composition on the thermodynamics of the formation of the η-phase. There is long standing concern regarding the effect of high Zn and low Cu content on the SCC performance of 7xxx alloys [2,15,19,74]. For instance, Holroyd and Scamans [74] have proposed empirical guidelines for optimizing SCC resistance in saline environments that includes suggesting alloy compositions should not exceed 8 wt.% Zn and remark that overageing becomes less effective as the Zn level is increased. Additionally, it has been demonstrated that new generation higher Zn content thick plate alloys like AA7085 have a significantly higher susceptibility to environmentally assisted cracking, compared to the more established AA7050 alloy, in overaged tempers [15]. It is well known that the incorporation of Cu in the η-phase can reduce the electrochemical difference between the matrix and precipitates, and hence effectively minimise its extent of anodic dissolution [18,19]. Higher Zn level in the matrix is thus expected to impact the electrochemical performance of 7xxx alloys through affecting the Cu content in the η-phase. Among the three alloys studied in the present work (AA7050, AA7010, and AA7085), the Cu content of the η-phase was predicted to be the highest for AA7050 which has the highest nominal Cu content, and lowest for AA7085, being 13 at.% and 9 at.% at 180 °C, respectively. The matrix residual Cu content was instead predicted to be the highest for AA7085, despite it con-

tained the lowest Cu content in the η-phase. Moreover, the matrix residual Zn content in AA7085 was almost 4 times higher than in AA7050. If the equilibrium matrix Zn content in AA7085 is artificially decreased from 1.1 at.% to 0.3 at.%, the chemical potential of Zn exhibits a considerable drop by 20%, from -24387Jmol^{-1} to -29039Jmol^{-1}, while the related chemical potential of Cu is nearly unaffected. Therefore, the high nominal Zn content in AA7085 has significantly enhanced the chemical potential of Zn, but with a minor influence on the counterpart of Cu, which essentially resulted in the higher Zn content in the η-phase, if the diffusion kinetics allow equilibrium to be achieved. As a result, the empirical fact that the benefits of overageing for avoiding SCC become less effective as the Zn level is increased can be partly ascribed to the gradual lowing of the Cu content in the η-phase with increasing nominal Zn content.

It is widely acknowledged that overageing with controlled heating rates and two or more isothermal stages can improve the SCC resistance of 7xxx alloys, mainly through enhancing the Cu content found in the η-phase after heat treatments at higher temperatures [15,74,78]. However, when increasing the ageing temperature in the range of commercial heat treatments, from 120 °C to 180 °C, the equilibrium Cu concentrations of the η-phase in both AA7050 and AA7085 are predicted to be only slightly increased (around 1 at.%), based on CALPHAD thermodynamic calculations. The above equilibrium calculations thus reveal that higher ageing temperatures during the overageing stage (*e.g.* at 180 °C) play only a minor role in the thermodynamics of the formation of the η-phase, from the perspective of the η-phase equilibrium solute compositions.

Since solute migration energies are an exponential function of temperature, increasing the ageing temperature is able to considerably enhance the solute diffusivity. For example, the diffusivities of all the solute elements (Cu, Mg, Zn) in AA7050 are enhanced by two orders of magnitude when increasing the ageing temperature from 120 °C to 180 °C. Ageing temperature is hence expected to play a much more important role in the kinetics of the η-phase formation, relative to its thermodynamic influence. The two-step ageing simulation (Fig. 10) indicates that the residual Cu matrix content was significantly supersaturated after the first ageing step at 120 °C for 24 h, while the Zn solute in the matrix has almost been completely depleted over the same time-scale. Correspondingly, the η-phase Cu content after 24 h ageing at 120 °C was only around 6 at.%, which is half of its equilibrium concentration of 12.5 at.% at 120 °C. This reveals that, after the first ageing step, although there is a large thermodynamic driving force for Cu atoms migrating from the supersaturated matrix to the η-phase, the kinetics of Cu enrichment in the η-phase is considerably limited by the low Cu diffusivity at 120 °C. As discussed above, increasing the ageing temperature from 120 °C to 180 °C has only a very subtle influence on the equilibrium η-phase Cu content in AA7050. In contrast, the rapid depletion and enrichment of Cu seen in the matrix and η-phase, respectively, after the second ageing step at 180 °C, has confirmed that the enrichment of Cu in the η-phase during overageing is essentially related to enhanced Cu diffusivity at higher temperatures. In addition, since the matrix Zn atoms have almost been completely depleted during the first ageing step, the matrix residual Zn content was only slightly affected by the second ageing step at 180 °C. Furthermore, both APT characterisation [20] and previous phase-field simulations [13] have revealed a pronounced Cu gradient confined within the PFZ region near GBs after 24 h ageing at 120 °C in a model AA7050 alloy; *i.e.* there was still a large difference in the Cu content in the matrix and within PFZ regions. The rapid depletion of Cu atoms in the matrix during the second ageing stage at 180 °C, as predicted in the present work, can thus pronouncedly minimize the Cu distribution difference (and consequently the electrochemical potential disparity) in the matrix and within PFZ regions. Therefore, the improvement of SCC resistance after overageing at high temperatures (*e.g.* 180 °C) can be generally ascribed to both the enhanced Cu content in the η-phase and the homogenised Cu partitioning within the PFZ regions and the matrix.

Although overageing for 7xxx alloys is usually employed at relatively higher temperatures [2,74,78], *e.g.* ranging from 150 °C to 180 °C, mainly to enhance Cu transport kinetics (as shown in Fig. 11), it has been recently reported that prolonged ageing of 150 h at 120 °C can also effectively reduce the corrosion propensity caused by the peak-ageing treatment (24 h at 120 °C) in AA7050 [72]. This is again expected to be related to the more gradual Cu incorporation in the η-phase during long artificial ageing at 120 °C. The present isothermal ageing simulation at 120 °C for AA7050 (Fig. 11) has confirmed that notable Cu enrichment in the η-phase (10 at.%) can indeed be successfully achieved after such long ageing times of 130 h at 120 °C. This implies that the η-phase in AA7050 at 120 °C has a relatively high equilibrium Cu content (*e.g.* 12.5 at.% from the CALPHAD prediction), but Cu enrichment in the η-phase is essentially limited by the low Cu diffusivity.

5. Conclusions

The present work has constructed a chemical-potential-based CALPHAD-informed phase-field model capable of describing a multi-component and two-sublattice phase formation by directly integrating the compound energy formalism. This relied on semi-analytically inverting the Gibbs free energy of the ordered phase, which allowed reformulation of the transport equation in terms of the diffusion potential rather than the composition as the field variable. Since the diffusion potentials are readily available in this formulation, the site fractions in each sublattice can be obtained through a direct forward calculation, thus avoiding computationally intensive constrained energy minimization procedures. While the model is outlined for a two-sublattice phase in this work, the approach is more general and can be easily extended to describe other multi-sublattice phases.

The developed model was employed to study the complex pathways for compositional evolution during the growth of the η-phase in commercially important Al-Zn-Mg-Cu alloys during heat treatment. We have systematically investigated the influence of alloy composition, solute diffusivity, and heat treatment parameters on the compositional evolution of the η-phase. Although simplifying assumptions on the interface energy and misfit strain were used in this work, it builds on well established CALPHAD-based mean-field precipitation models [79] by including long-range diffusional effects and precipitate interactions. The results predicted that the compositional evolution of the η-phase during the ageing process in all the three alloys (AA7050, AA7010, AA7085) studied were characterised by the simultaneous enrichment of Cu and Al in the η-phase, accompanied by the gradual depletion of Zn, which thermodynamically favours the stabilization of the ordered Laves-C14 structure of the η-phase. Through comparing the η-phase growth kinetics and the matrix residual solute evolution in AA7050, it was found that Zn exhaustion mainly controlled the η-phase growth process during the early stage of ageing, resulting in fast η-phase growth kinetics, enrichment of Zn in the η-phase, and an excess in the residual Cu solute in the matrix. The gradual enrichment of Cu in the η-phase subsequently occurred during the later ageing stage and was in principle kinetically controlled, due to the slower diffusivity of Cu relative to Zn in the matrix. The thermodynamic calculations revealed that the higher nominal Zn composition in AA7085 relative to AA7050 could significantly enhance the chemical potential of Zn, but had a minor influence on Cu, which essentially resulted in a higher Zn content (and consequently lower Cu) in the η-phase. Two-step ageing simulation of AA7050 suggested that the matrix was almost completely depleted of Zn after the first ageing

step for 24 h at 120 °C, whilst remaining highly supersaturated in Cu. Subsequent higher temperature ageing (at 180 °C) thus significantly enhanced the incorporation of Cu atoms from the supersaturated matrix into the η-phase, while it had little influence on the matrix residual Zn content.

Declaration of Competing Interest

The authors declare that they have no known competing financial interests or personal relationships that could have appeared to influence the work reported in this paper.

Acknowledgements

CL and PS are grateful to the DFG for financial support through subproject M5 in the Priority Programme SPP 1713: Strong Coupling of Thermo-chemical and Thermo-mechanical States in Applied Materials. CL acknowledges the kind support by Shanghai Jiao Tong University through the Outstanding Graduate Student program. PS and PBP are also grateful to the EPSRC for financial support through the associated programme grant LightFORM (EP/R001715/1) and the Airbus–University of Manchester Centre for Metallurgical Excellence, UK for supporting aspects of this research.

Supplementary material

Supplementary material associated with this article can be found, in the online version, at doi:10.1016/j.actamat.2021.117602.

References

[1] R.C. Reed, The Superalloys: Fundamentals and Applications, Cambridge University Press, 2008.
[2] J.C. Williams, E.A. Starke Jr, Progress in structural materials for aerospace systems, Acta Mater. 51 (19) (2003) 5775–5799.
[3] G. Sha, A. Cerezo, Early-stage precipitation in Al–Zn–Mg–Cu alloy (7050), Acta Mater. 52 (15) (2004) 4503–4516.
[4] W. Sun, Y. Zhu, R. Marceau, L. Wang, Q. Zhang, X. Gao, C. Hutchinson, Precipitation strengthening of aluminum alloys by room-temperature cyclic plasticity, Science 363 (2019) 972–975.
[5] F. Cao, J. Zheng, Y. Jiang, B. Chen, Y. Wang, T. Hu, Experimental and DFT characterization of η' nano-phase and its interfaces in AlZnMgCu alloys, Acta Mater. 164 (2019) 207–219.
[6] P. Dumitraschkewitz, S.S. Gerstl, L.T. Stephenson, P.J. Uggowitzer, S. Pogatscher, Clustering in age-hardenable aluminum alloys, Adv. Eng. Mater. 20 (10) (2018) 1800255.
[7] C. Hutchinson, Modeling the kinetics of precipitation in aluminium alloys, in: Fundamentals of Aluminium Metallurgy, Elsevier, 2011, pp. 422–467.
[8] P. Zhang, K. Shi, J. Bian, J. Zhang, Y. Peng, G. Liu, A. Deschamps, J. Sun, Solute cluster evolution during deformation and high strain hardening capability in naturally aged Al–Zn–Mg alloy, Acta Mater. 207 (2021) 116682.
[9] P. Dumitraschkewitz, P.J. Uggowitzer, S.S. Gerstl, J.F. Löffler, S. Pogatscher, Size-dependent diffusion controls natural aging in aluminium alloys, Nat. Commun. 10 (1) (2019) 1–6.
[10] J.-F. Nie, Physical metallurgy of light alloys, in: Physical Metallurgy, Elsevier, 2014, pp. 2009–2156.
[11] T.-F. Chung, Y.-L. Yang, B.-M. Huang, Z. Shi, J. Lin, T. Ohmura, J.-R. Yang, Transmission electron microscopy investigation of separated nucleation and in-situ nucleation in AA7050 aluminium alloy, Acta Mater. 149 (2018) 377–387.
[12] T.-F. Chung, Y.-L. Yang, M. Shiojiri, C.-N. Hsiao, W.-C. Li, C.-S. Tsao, Z. Shi, J. Lin, J.-R. Yang, An atomic scale structural investigation of nanometre-sized η precipitates in the 7050 aluminium alloy, Acta Mater. 174 (2019) 351–368.
[13] C. Liu, A. Garner, H. Zhao, P.B. Prangnell, B. Gault, D. Raabe, P. Shanthraj, CALPHAD-informed phase-field modeling of grain boundary microchemistry and precipitation in Al-Zn-Mg-Cu alloys, Acta Mater. 214 (2021) 116966.
[14] E. Clouet, L. Laé, T. Épicier, W. Lefebvre, M. Nastar, A. Deschamps, Complex precipitation pathways in multicomponent alloys, Nat. Mater. 5 (6) (2006) 482–488.
[15] E. Schwarzenböck, E. Ollivier, A. Garner, A. Cassell, T. Hack, Z. Barrett, C. Engel, T.L. Burnett, N.H. Holroyd, J.D. Robson, et al., Environmental cracking performance of new generation thick plate 7000-T7x series alloys in humid air, Corros. Sci. 171 (2020) 108701.
[16] T. Marlaud, A. Deschamps, F. Bley, W. Lefebvre, B. Baroux, Influence of alloy composition and heat treatment on precipitate composition in Al–Zn–Mg–Cu alloys, Acta Mater. 58 (2010) 248–260.
[17] T. Marlaud, A. Deschamps, F. Bley, W. Lefebvre, B. Baroux, Evolution of precipitate microstructures during the retrogression and re-ageing heat treatment of an Al-Zn-Mg-Cu alloy, Acta Mater. 58 (2010) 4814–4826.
[18] T. Ramgopal, P. Schmutz, G. Frankel, Electrochemical behavior of thin film analogs of Mg(Zn, Cu, Al)$_2$, J. Electrochem. Soc. 148 (2001) B348–B356.
[19] S. Knight, K. Pohl, N. Holroyd, N. Birbilis, P. Rometsch, B. Muddle, R. Goswami, S. Lynch, Some effects of alloy composition on stress corrosion cracking in Al-Zn-Mg-Cu alloys, Corros. Sci. 98 (2015) 50–62.
[20] H. Zhao, F. De Geuser, A.K. da Silva, A. Szczepaniak, B. Gault, D. Ponge, D. Raabe, Segregation assisted grain boundary precipitation in a model Al-Zn-Mg-Cu alloy, Acta Mater. 156 (2018) 318–329.
[21] A. Garner, R. Euesden, Y. Yao, Y. Aboura, H. Zhao, J. Donoghue, M. Curioni, B. Gault, P. Shanthraj, Z. Barrett, et al., Multiscale analysis of grain boundary microstructure in high strength 7xxx Al alloys, Acta Mater. 202 (2021) 190–210.
[22] A. Borgenstam, L. Höglund, J. Ågren, A. Engström, DICTRA, a tool for simulation of diffusional transformations in alloys, J. Phase Equilib. 21 (2000) 269.
[23] I.M. Lifshitz, V.V. Slyozov, The kinetics of precipitation from supersaturated solid solutions, J. Phys. Chem. Solids 19 (1–2) (1961) 35–50.
[24] L.-Q. Chen, Phase-field models for microstructure evolution, Annu. Rev. Mater. Res. 32 (2002) 113–140.
[25] I. Steinbach, M. Apel, Multi phase field model for solid state transformation with elastic strain, Physica D 217 (2006) 153–160.
[26] N. Moelans, B. Blanpain, P. Wollants, An introduction to phase-field modeling of microstructure evolution, Calphad 32 (2008) 268–294.
[27] Y. Wang, J. Li, Phase field modeling of defects and deformation, Acta Mater. 58 (2010) 1212–1235.
[28] B. Svendsen, P. Shanthraj, D. Raabe, Finite-deformation phase-field chemomechanics for multiphase, multicomponent solids, J. Mech. Phys. Solids 112 (2018) 619–636.
[29] C. Liu, P. Shanthraj, M. Diehl, F. Roters, S. Dong, J. Dong, W. Ding, D. Raabe, An integrated crystal plasticity–phase field model for spatially resolved twin nucleation, propagation, and growth in hexagonal materials, Int. J. Plast. 106 (2018) 203–227.
[30] C. Liu, P. Shanthraj, J.D. Robson, M. Diehl, S. Dong, J. Dong, W. Ding, D. Raabe, On the interaction of precipitates and tensile twins in magnesium alloys, Acta Mater. 178 (2019) 146–162.
[31] P. Shanthraj, C. Liu, A. Akbarian, B. Svendsen, D. Raabe, Multi-component chemo-mechanics based on transport relations for the chemical potential, Comput. Methods Appl. Mech. Eng. 365 (2020) 113029.
[32] H.L. Lukas, S.G. Fries, B. Sundman, Computational Thermodynamics: The Calphad Method, vol. 131, Cambridge university press Cambridge, 2007.
[33] J. Ågren, Calculation of phase diagrams: calphad, Curr. Opin. Solid State Mater. Sci. 1 (1996) 355–360.
[34] U. Grafe, B. Bottger, J. Tiaden, S. Fries, Coupling of multicomponent thermodynamic databases to a phase field model: application to solidification and solid state transformations of superalloys, Scr. Mater. 42 (2000) 1179–1186.
[35] J. Zhu, Z. Liu, V. Vaithyanathan, L. Chen, Linking phase-field model to CALPHAD: application to precipitate shape evolution in Ni-base alloys, Scr. Mater. 46 (5) (2002) 401–406.
[36] K. Grönhagen, J. Ågren, M. Odén, Phase-field modelling of spinodal decomposition in TiAlN including the effect of metal vacancies, Scr. Mater. 95 (2015) 42–45.
[37] S.G. Kim, W.T. Kim, T. Suzuki, Phase-field model for binary alloys, Phys. Rev. E 60 (1999) 7186.
[38] J. Eiken, B. Böttger, I. Steinbach, Multiphase-field approach for multicomponent alloys with extrapolation scheme for numerical application, Phys. Rev. E 73 (2006) 066122.
[39] J. Zhu, T. Wang, A. Ardell, S. Zhou, Z. Liu, L. Chen, Three-dimensional phase–field simulations of coarsening kinetics of γ' particles in binary Ni–Al alloys, Acta Mater. 52 (2004) 2837–2845.
[40] K. Wu, Y. Chang, Y. Wang, Simulating interdiffusion microstructures in Ni–Al–Cr diffusion couples: a phase field approach coupled with CALPHAD database, Scr Mater 50 (2004) 1145–1150.
[41] Y. Gao, N. Zhou, F. Yang, Y. Cui, L. Kovarik, N. Hatcher, R. Noebe, M. Mills, Y. Wang, P-phase precipitation and its effect on martensitic transformation in (Ni, Pt) Ti shape memory alloys, Acta Mater. 60 (2012) 1514–1527.
[42] L. Zhang, M. Stratmann, Y. Du, B. Sundman, I. Steinbach, Incorporating the CALPHAD sublattice approach of ordering into the phase-field model with finite interface dissipation, Acta Mater. 88 (2015) 156–169.
[43] I. Steinbach, L. Zhang, M. Plapp, Phase-field model with finite interface dissipation, Acta Mater. 60 (2012) 2689–2701.
[44] T. Kitashima, Coupling of the phase-field and CALPHAD methods for predicting multicomponent, solid-state phase transformations, Philos. Mag. 88 (11) (2008) 1615–1637.
[45] T. Kitashima, H. Harada, A new phase-field method for simulating γ' precipitation in multicomponent nickel-base superalloys, Acta Mater. 57 (2009) 2020–2028.
[46] A. Rahnama, R. Dashwood, S. Sridhar, A phase-field method coupled with CALPHAD for the simulation of ordered κ-carbide precipitates in both disordered γ and α phases in low density steel, Comput. Mater. Sci 126 (2017) 152–159.
[47] A. Rahnama, H. Kotadia, S. Sridhar, Effect of Ni alloying on the microstructural evolution and mechanical properties of two duplex light-weight steels during different annealing temperatures: experiment and phase-field simulation, Acta Mater. 132 (2017) 627–643.
[48] M. Plapp, Unified derivation of phase-field models for alloy solidification from a grand-potential functional, Phys. Rev. E 84 (2011) 031601.

[49] A. Choudhury, B. Nestler, Grand-potential formulation for multicomponent phase transformations combined with thin-interface asymptotics of the double-obstacle potential, Phys. Rev. E 85 (2) (2012) 021602.
[50] S. Chatterjee, N. Moelans, A grand-potential based phase-field approach for simulating growth of intermetallic phases in multicomponent alloy systems, Acta Mater. 206 (2021) 116630.
[51] I. Steinbach, F. Pezzolla, B. Nestler, M. Seeßelberg, R. Prieler, G.J. Schmitz, J.L. Rezende, A phase field concept for multiphase systems, Physica D 94 (1996) 135–147.
[52] J. Tiaden, B. Nestler, H.-J. Diepers, I. Steinbach, The multiphase-field model with an integrated concept for modelling solute diffusion, Physica D 115 (1998) 73–86.
[53] B. Nestler, A. Wheeler, A multi-phase-field model of eutectic and peritectic alloys: numerical simulation of growth structures, Physica D 138 (2000) 114–133.
[54] M. Hillert, Phase Equilibria, Phase Diagrams and Phase Transformations: Their Thermodynamic Basis, Cambridge University Press, 2007.
[55] F. Roters, M. Diehl, P. Shanthraj, P. Eisenlohr, C. Reuber, S.L. Wong, T. Maiti, A. Ebrahimi, T. Hochrainer, H.-O. Fabritius, et al., DAMASK–the Düsseldorf advanced material simulation kit for modeling multi-physics crystal plasticity, thermal, and damage phenomena from the single crystal up to the component scale, Comput. Mater. Sci 158 (2019) 420–478.
[56] S. Balay, S. Abhyankar, M.F. Adams, J. Brown, P. Brune, K. Buschelman, L. Dalcin, A. Dener, V. Eijkhout, W.D. Gropp, D. Karpeyev, D. Kaushik, M.G. Knepley, D.A. May, L.C. McInnes, R.T. Mills, T. Munson, K. Rupp, P. Sanan, B.F. Smith, S. Zampini, H. Zhang, H. Zhang, PETSc Users Manual, Technical Report ANL-95/11 - Revision 3.14, Argonne National Laboratory, 2020.
[57] N. Saunders, COST 507: Thermochemical Database for Light Metal Alloys, European Commission, Brussels, Belgium, 1998, pp. 23–27.
[58] E. Kozeschnik, B. Buchmayr, MatCalc–a simulation tool for multicomponent thermodynamics, diffusion and phase transformation kinetics, in: H. Cerjak, H.K.D.H. Bhadeshia (Eds.), Mathematical Modelling of Weld Phenomena, vol. 5, Institute of Materials, 2001, pp. 349–361.
[59] X. Fang, Y. Du, M. Song, K. Li, C. Jiang, Effects of Cu content on the precipitation process of Al–Zn–Mg alloys, J. Mater. Sci. 47 (23) (2012) 8174–8187.
[60] M. Perez, Gibbs–thomson effects in phase transformations, Scr. Mater. 52 (8) (2005) 709–712.
[61] J. Park, Influence of retrogression and reaging treatments on the strength and stress corrosion resistance of aluminium alloy 7075-T6, Mater. Sci. Eng. A 103 (2) (1988) 223–231. A Structural Materials: Properties, Microstructure and Processing
[62] J. Li, N. Birbilis, C. Li, Z. Jia, B. Cai, Z. Zheng, Influence of retrogression temperature and time on the mechanical properties and exfoliation corrosion behavior of aluminium alloy AA7150, Mater. Charact. 60 (11) (2009) 1334–1341.
[63] M. Islam, W. Wallace, Stresscorrosion-rack grovvth behaviour of 7475 T6 retrogressed and reaged aluminium alloy, Metals Technol. 11 (1) (1984) 320–322.
[64] M. Islam, W. Wallace, Retrogression and reaging response of 7475 aluminium alloy, Metals Technol. 10 (1) (1983) 386–392.
[65] F. Viana, A. Pinto, H. Santos, A. Lopes, Retrogression and re-ageing of 7075 aluminium alloy: microstructural characterization, J. Mater. Process. Technol. 92–93 (1999) 54–59.
[66] M. Talianker, B. Cina, Retrogression and reaging and the role of dislocations in the stress corrosion of 7000-type aluminum alloys, Metall. Trans. A 20 (10) (1989) 2087–2092.
[67] Y.-P. Xiao, Q.-L. Pan, W.-B. Li, X.-Y. Liu, Y.-B. He, Influence of retrogression and re-aging treatment on corrosion behaviour of an Al–Zn–Mg–Cu alloy, Mater. Des. 32 (4) (2011) 2149–2156.
[68] J.A. Österreicher, F. Grabner, M.A. Tunes, D.S. Coradini, S. Pogatscher, C.M. Schlögl, Two step–ageing of 7xxx series alloys with an intermediate warm-forming step, J. Mater. Res. Technol. 12 (2021) 1508–1515.
[69] J.A. Österreicher, M.A. Tunes, F. Grabner, A. Arnoldt, T. Kremmer, S. Pogatscher, C.M. Schlögl, Warm-forming of pre-aged Al–Zn–Mg–Cu alloy sheet, Mater. Des. 193 (2020) 108837.
[70] T.M. Kremmer, P. Dumitraschkewitz, D. Pöschmann, T. Ebner, P.J. Uggowitzer, G.K. Kolb, S. Pogatscher, Microstructural change during the interrupted quenching of the AlZnMg(Cu) alloy AA7050, Materials 13 (11) (2020) 2554.
[71] K. Stiller, P. Warren, V. Hansen, J. Angenete, J. Gjønnes, Investigation of precipitation in an Al–Zn–Mg alloy after two-step ageing treatment at 100 and 150 °C, Mater. Sci. Eng. A 270 (1) (1999) 55–63.
[72] F. Song, X. Zhang, S. Liu, Q. Tan, D. Li, The effect of quench rate and overageing temper on the corrosion behaviour of AA7050, Corros. Sci. 78 (2014) 276–286.
[73] H. Zhao, B. Gault, D. Ponge, D. Raabe, Reversion and re-aging of a peak aged Al-Zn-Mg-Cu alloy, Scr. Mater. 188 (2020) 269–273.
[74] N.H. Holroyd, G. Scamans, Stress corrosion cracking in Al-Zn-Mg-Cu aluminum alloys in saline environments, Metall. Mater. Trans. A 44 (3) (2013) 1230–1253.
[75] G. Sha, Y. Wang, X. Liao, Z. Duan, S. Ringer, T. Langdon, Influence of equal-channel angular pressing on precipitation in an Al–Zn–Mg–Cu alloy, Acta Mater. 57 (10) (2009) 3123–3132.
[76] Y. Zhang, S. Jin, P.W. Trimby, X. Liao, M.Y. Murashkin, R.Z. Valiev, J. Liu, J.M. Cairney, S.P. Ringer, G. Sha, Dynamic precipitation, segregation and strengthening of an Al-Zn-Mg-Cu alloy (AA7075) processed by high-pressure torsion, Acta Mater. 162 (2019) 19–32.
[77] M. Styles, T. Bastow, M. Gibson, C. Hutchinson, Substitution of Cu and/or Al in η phase (MgZn2) and the implications for precipitation in Al–Zn–Mg–(Cu) alloys, Intermetallics 49 (2014) 40–51.
[78] A.U. Rao, V. Vasu, M. Govindaraju, K.S. Srinadh, Stress corrosion cracking behaviour of 7xxx aluminum alloys: a literature review, Trans. Nonferrous Metals Soc. China 26 (6) (2016) 1447–1471.
[79] Q. Chen, K. Wu, G. Sterner, P. Mason, Modeling precipitation kinetics during heat treatment with calphad-based tools, J. Mater. Eng. Perform. 23 (12) (2014) 4193–4196.